

## Supporting Information

### Multiple Heteroatom Substitution Effect on Destructive Quantum Interference in Tripodal Single-Molecule Junctions

Fa-Yu Qu,<sup>ab</sup> Zhi-Hao Zhao,<sup>bc</sup> Xiao-Rui Ren,<sup>bc</sup> Shou-Feng Zhang<sup>d</sup>, Lin Wang<sup>\*a</sup>  
and Dong Wang<sup>\*bc</sup>

<sup>a</sup> *School of Materials Science and Technology, China University of Geosciences, Beijing, 10083, China. E-mail: [wanglin712@cugb.edu.cn](mailto:wanglin712@cugb.edu.cn)*

<sup>b</sup> *CAS Key Laboratory of Molecular Nanostructure and Nanotechnology and Beijing National Laboratory for Molecular Sciences, Institute of Chemistry, Chinese Academy of Science (CAS), Beijing, 100190, China. E-mail: [wangd@iccas.ac.cn](mailto:wangd@iccas.ac.cn)*

<sup>c</sup> *University of Chinese Academy of Sciences, Beijing, 100049, China.*

<sup>d</sup> *Department of Electronic Engineering, Guangxi University of Science and Technology, Liuzhou, 545006, P. R. China.*

# Table of Contents

## **I. Theoretical Simulation**

- a. General Methods and Details
- b. Additional Data and Figures

## **II. STM-Break Junction Experiments**

- a. Experimental Details
- b. Data Analysis
- c. Supplemental Single-Molecule Conductance Experiments

## **III. Supplemental Notes**

- a. Discussion about the extremely low conductance of the molecule 0N-3NH<sub>2</sub>
- b. Discussion about the anchor-independent conductance of the 3N series
- c. Comparison with previous work by Solomon et al
- d. Extended curly arrow rules to rationalize the structural effects on DQI
- e. Discussion on the experimental conductance of 3N-3SMe and 2N-3SMe

## **IV. Synthesis and Characterization of the Molecules**

## **V. References**

## I. Theoretical Simulation

### a. General Methods and Details

The HMO distributions were calculated and depicted using HuLiS software package.<sup>1, 2</sup> All the optimized procedure and the transmission calculations were performed using Atomistix ToolKit (ATK) and Virtual NanoLab software packages 13.8.0. Free molecule was firstly optimized to a force threshold of 0.01 eV/Å for all atoms using DFT. The exchange correlation functional was generalized gradient approximation (GGA). Subsequently, to construct a molecular device, we introduced the molecule between a four-atom pyramid on the gold surfaces with a (7×7) super cell. As an initial guess, the thiomethyl group was chosen to locate on the adatom site with an Au-S bond length of 2.35 Å.<sup>3</sup> For the molecules **0~3N-3NH<sub>2</sub>**, the amino group was chosen to locate on the adatom site with an Au-N bond length of 2.36 Å and a C-N-Au angle of 121.31 degrees.<sup>4</sup> For structural optimization of the two-terminal devices, we constrained all the Au electrode atoms in their bulk positions and optimized the molecular system until all maximum forces on each atom were smaller than 0.05 eV/Å. In the optimization process, two k-points in the irreducible part of the Brillouin zone for the x- and y-directions, and one k-point for the z-direction (the transport direction of the junction). Double-ζ (DZ) basis set for Au atoms and double-zeta plus polarization (DZP) basis set for the molecules were adopted in the calculation.<sup>5</sup> Then electron transport calculations of the device were performed by DFT combined with the non-equilibrium Green's function (NEGF) method. The mesh-cutoff energy was set at 75 Hartree and k-points sampling (1×1×200) was adopted for x, y and z direction, respectively. GGA was used as exchange correlation functional.

## b. Additional Data and Figures

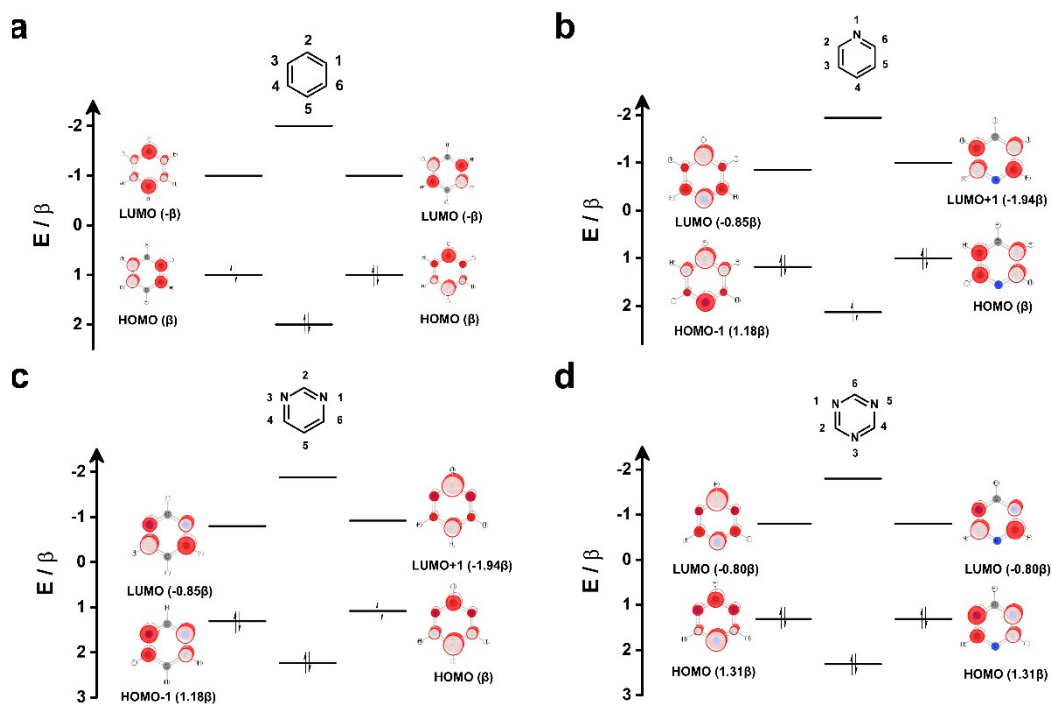


Figure S1. Molecular orbitals diagram near  $E_F$  of benzene, pyridine, 1,3-diazine and triazine.

**Table S1.** MO energies and coefficients at specific atom sites for benzene

E	$\alpha+2.00\beta$	$\alpha+1.00\beta$	$\alpha+1.00\beta$	$\alpha-1.00\beta$	$\alpha-1.00\beta$	$\alpha-2.00\beta$
1 C	0.41	-0.5	0.29	-0.5	-0.29	-0.41
2 C	0.41	-0.5	-0.29	0.5	-0.29	0.41
3 C	0.41	0	-0.58	0	0.58	-0.41
4 C	0.41	0.5	-0.29	-0.5	-0.29	0.41
5 C	0.41	0.5	0.29	0.5	-0.29	-0.41
6 C	0.41	0	0.58	0	0.58	0.41

**Table S2.** MO energies and coefficients at specific atom sites for pyridine

E	$\alpha+2.13\beta$	$\alpha+1.18\beta$	$\alpha+1.00\beta$	$\alpha-0.85\beta$	$\alpha-1.00\beta$	$\alpha-1.94\beta$
1 N	0.53	-0.56	-0.00	-0.54	-0.00	0.33
2 C	0.42	-0.18	-0.50	0.36	-0.50	-0.40
3 C	0.35	0.36	-0.50	0.24	0.50	0.43
4 C	0.33	0.60	0.00	-0.57	-0.00	-0.45
5 C	0.35	0.36	0.50	0.24	-0.50	0.43
6 C	0.42	-0.18	0.50	0.36	0.50	-0.40

**Table S3.** MO energies and coefficients at specific atom sites for 1,3-diazine

E	$\alpha+2.23\beta$	$\alpha+1.31\beta$	$\alpha+1.08\beta$	$\alpha-0.80\beta$	$\alpha-0.92\beta$	$\alpha-1.88\beta$
1 N	0.47	0.56	0.26	0.44	-0.3	-0.35
2 C	0.43	0	0.49	0	0.66	0.38
3 N	0.47	-0.56	0.26	-0.44	-0.3	-0.35
4 C	0.36	-0.44	-0.34	0.56	-0.24	0.44
5 C	0.33	0	-0.63	0	0.52	-0.47
6 C	0.36	0.44	-0.34	-0.56	-0.24	0.44

**Table S4.** MO energies and coefficients at specific atom sites for 1,3,5-triazine

E	$\alpha+2.31\beta$	$\alpha+1.31\beta$	$\alpha+1.31\beta$	$\alpha-0.80\beta$	$\alpha-0.80\beta$	$\alpha-1.80\beta$
1 N	-0.43	0.32	0.56	0.25	0.44	-0.38
2 C	-0.38	-0.25	0.44	0.32	-0.56	0.43
3 N	-0.43	-0.64	0	-0.5	0	-0.38
4 C	-0.38	-0.25	-0.44	0.32	0.56	0.43
5 N	-0.43	0.32	-0.56	0.25	-0.44	-0.38
6 C	-0.38	0.5	0	-0.64	0	0.43

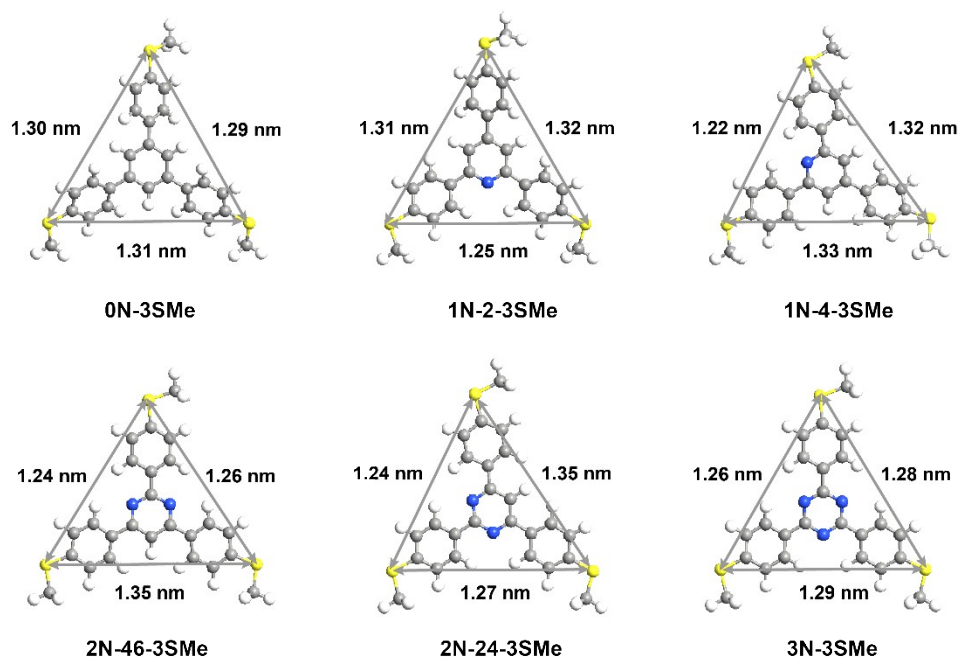


**Figure S2.** Optimized molecule structure of the target molecules calculated based on DFT. The arrow shows the distance between S-S atoms. The slightly different S-S distances between **1N-2-3SMe** and **1N-4-3SMe** (or **2N-46-3SMe** and **2N-24-3SMe**) stems from the original conformation of thiomethyl (-SMe) substituents.

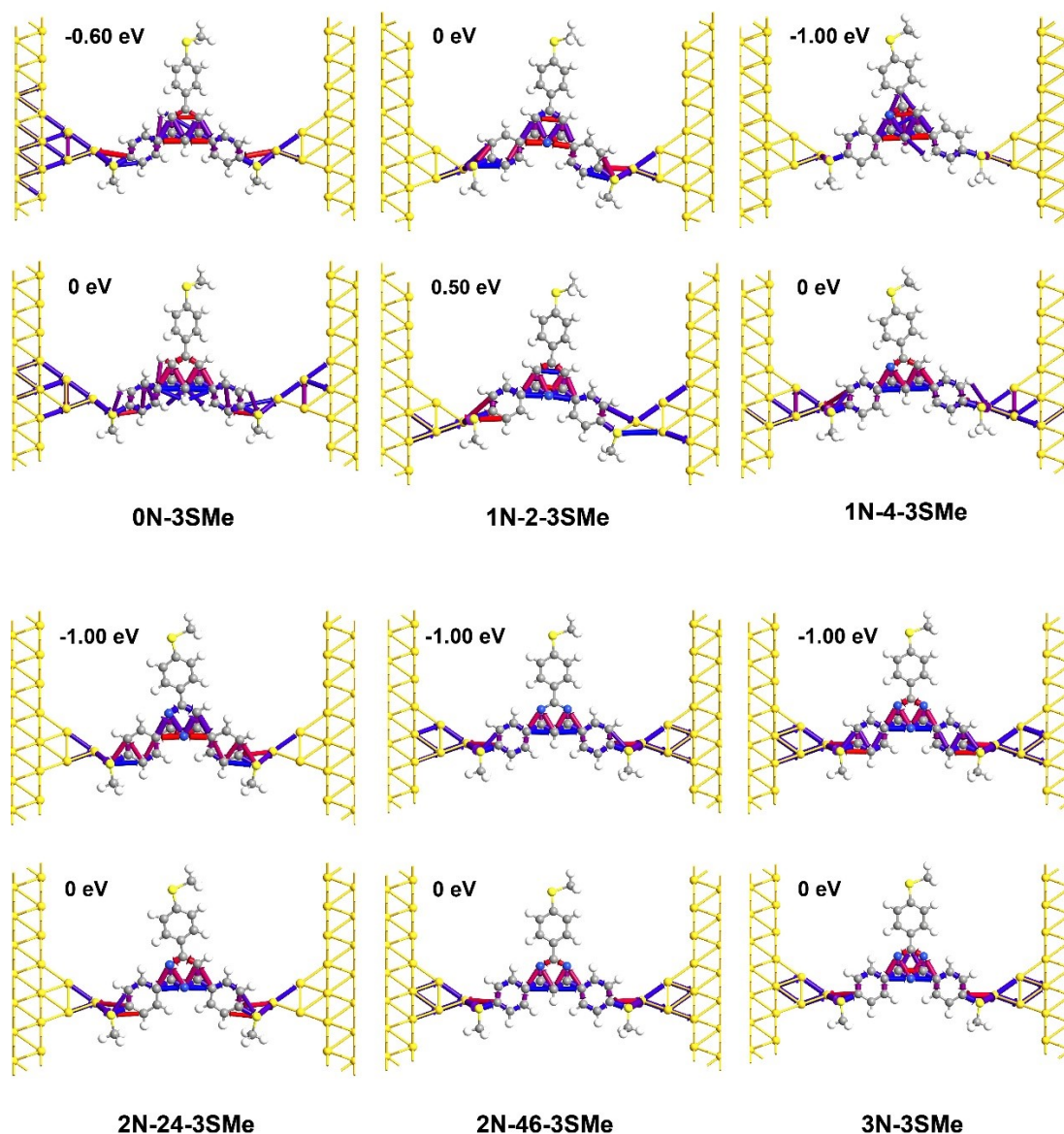


**Figure S3.** Interatomic transmission pathways based on the calculated transmission spectra of the *meta*-substituted 0N-3SMe, 1N-2-3SMe, 1N-4-3SMe, 2N-24-3SMe, 2N-46-3SMe and 3N-3SMe molecules. An arrow is only drawn when the magnitude of the local transmission between a pair of atoms is at least 10% of the maximum local transmission at that energy. The red arrows indicate the transmission that are in the direction of the net current flow, thereby contributing to the current, whereas the blue arrows give the transmission in the opposite direction, thereby reducing the net current.

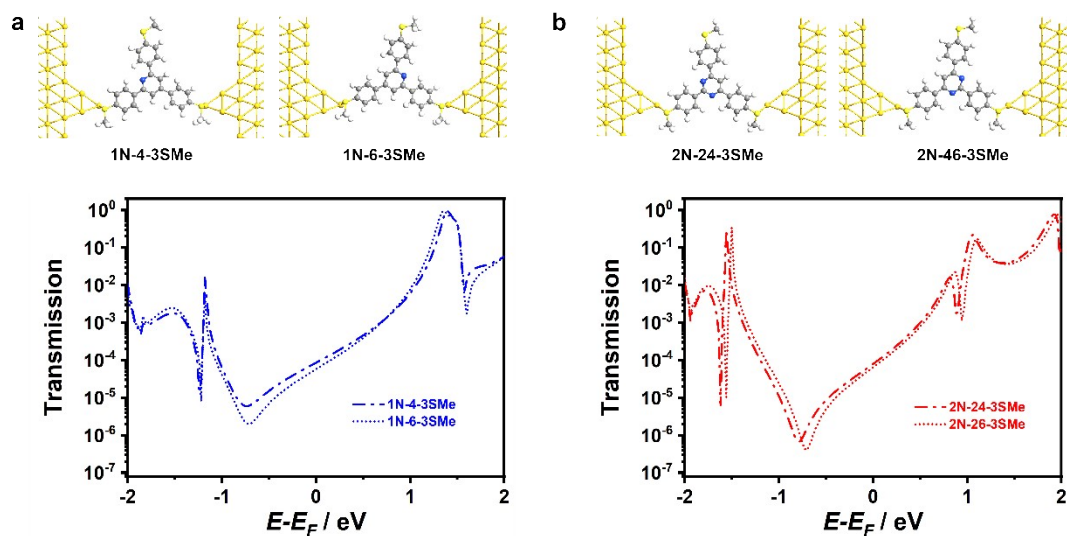


**Figure S4.** Geometric structures and transmission spectra of (a)1N-4-3SMe and 1N-3SMe-6 (b) 2N-24-3SMe and 2N-3SMe-26. Only slight difference can be observed but the moving direction of anti-resonance valley relative to Fermi level does not change with the substituted site.

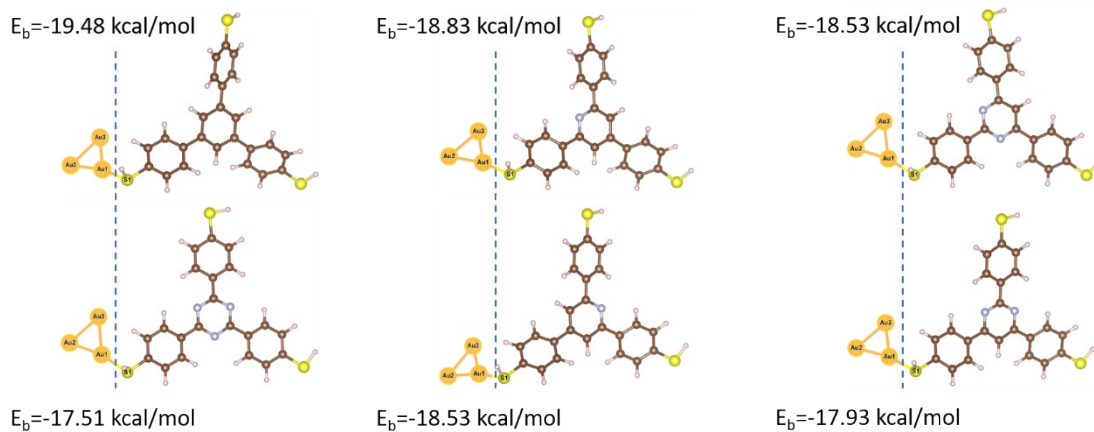


**Figure S5.** The Au-S binding energy calculated based on Au←SH coordination bond.



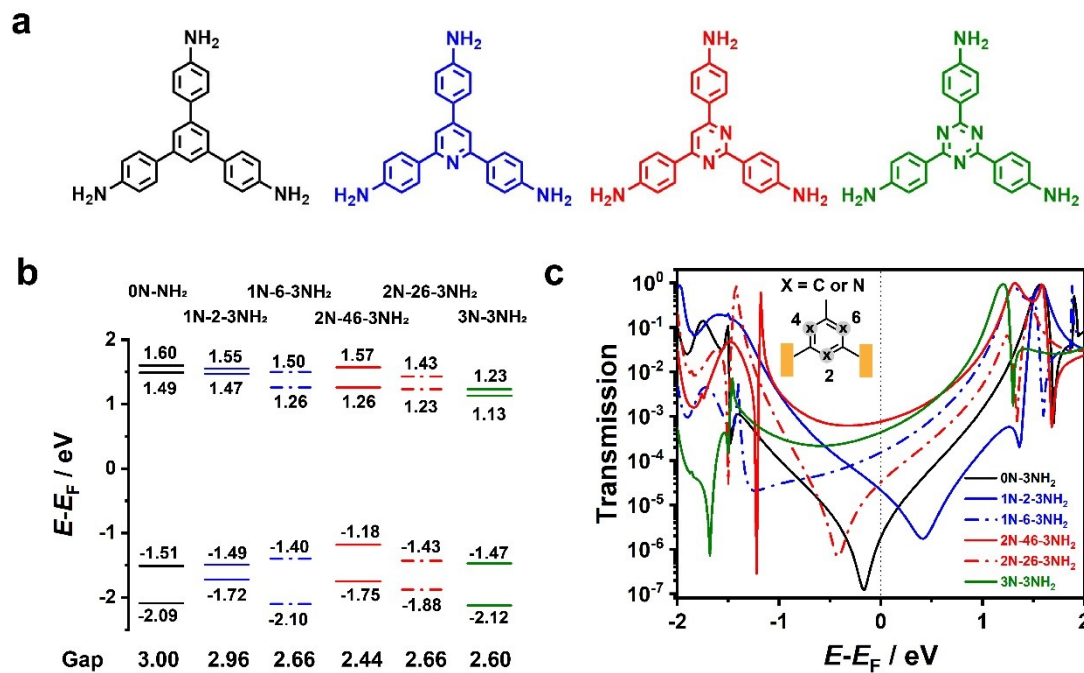


**Figure S6.** (a) Molecular structures, (b) frontier orbital energy (in eV) of HOMO-1, HOMO, LUMO and LUMO+1 and (c) transmission spectra for **0-3N-3NH<sub>2</sub>**. The inset shows the schematic configuration of the molecular junction in which two anchor groups are connected with the electrodes with the third one pendent.

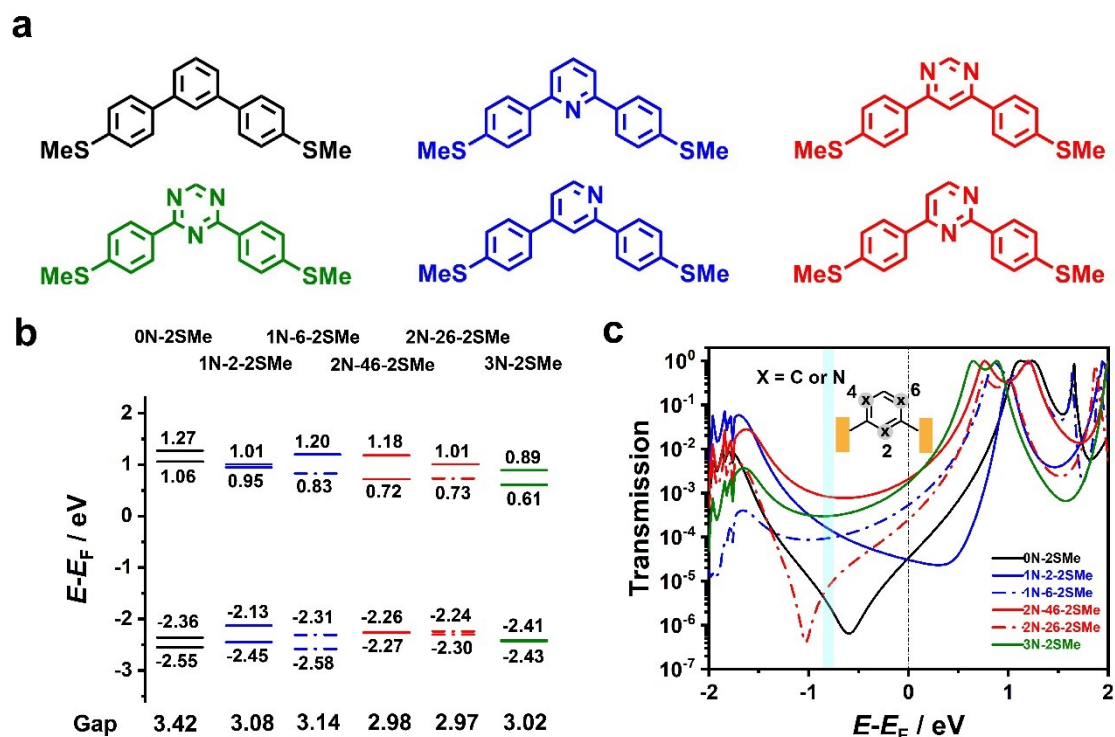


**Figure S7.** (a) Molecular structures, (b) frontier orbital energy (in eV) of HOMO-1, HOMO, LUMO

and LUMO+1 and (c) transmission spectra for **0-3N-2SMe**. Note that the molecules are different from those in the main manuscript which have only two anchoring groups. The dash line at 0 eV indicates the calculated Fermi level by DFT. The cyan stripe at around -0.8 eV shows the Fermi energy at which the calculated conductance values are in qualitative agreement with the experimental findings.

## II. STM-Break Junction Experiments

### a. Experimental Details

Single-molecule conductance measurements were carried out using Xtech STM-BJ developed by Prof. Wenjing Hong's group<sup>6</sup>, and the data is analyzed by XMe open-source code ([https://github.com/Pilab-XMU/XMe\\_DataAnalysis](https://github.com/Pilab-XMU/XMe_DataAnalysis)).

The Au substrate was prepared by evaporating ~100 nm Au onto silicon wafer (purchased from Beijing Topvender Technology Co., Ltd.) and then cleaned by piranha solution (7:3 concentrated H<sub>2</sub>SO<sub>4</sub>/H<sub>2</sub>O<sub>2</sub>) before each experiment. The gold tip was made by flame cleaning of gold wires (0.25 nm diameter, Pram Corporation, 99.99%) to form a gold bead.<sup>7</sup> The conductance of the objective molecules was measured in a Teflon cell filled with 0.1 mM molecular solution (volume ratio of the mixed solvent, V<sub>THF</sub>: V<sub>TMB</sub> = 1:4) in the ambient atmosphere. The cell was preliminarily dipped in piranha solution and then washed by sonication in Milli-Q water (18.2 MΩ, TOC ≤4 ppb) for several times. All the solvents, including tetrahydrofuran (THF; TCI, 99% purity), mesitylene (TMB; J&K, 98% purity) and dichloromethane (DCM; J&K, 99.8% purity) were purchased directly used without further purification.

For each molecule, we repeatedly formed and broke Au point contacts with the tip approaching/retracting at the speed of 10 nm/s and recorded the traces of conductance versus displacement as the tip was withdrawn. We collected more than 2000 traces for every measurement at different positions of the substrate. Data in each experiment was acquired and analyzed with a lab-made program in Labview 2016. All the traces were recorded consecutively and automatically without data selection. At least two independent experiments were conducted to ensure that the results are reproducible.

## b. Data Analysis

In one-dimensional (1D) histogram, we can observe several sharp statistical peaks corresponding to  $G_0$ ,  $2G_0$ ,  $3G_0 \dots$ , indicating that the gold electrodes break step by step and the atomic interface has been formed facilitating the single-molecule measurement. Below the gold quantum contact, the most probable conductance peak was fitted by Gaussian distribution.

Then, we compiled all the conductance-displacement traces to construct the two-dimensional (2D) histogram, from which the geometric information of the molecular junction can be deduced. We introduced a relative distance ( $\Delta z$ ) and defined  $\Delta z = 0$  at  $10^{-0.3} G_0$  to align all the stretching curves. Bright features, showing gold–gold contacts, can be seen around  $G = G_0$ , followed by another well-defined conductance scatter group in the range of  $10^{-3.0}$ – $10^{-6.0} G_0$ .

The stretching distance histograms are constructed according to the literature.<sup>6, 8</sup> Briefly, a starting point and an ending point are needed to determine the stretching distance. The starting point is the position where the conductance is  $10^{-0.3} G_0$  (after the rupture of the gold-gold atomic point contact at  $G_0$ ). After the connection between the molecule and the electrode breaks, the conductance decays rapidly. The turning point of the conductance curve in Fig. S8a is the ending point. The displacement difference between the starting and ending point is the stretching distance. Statistically, we choose the end of the conductance peak in the 1D diagram (Fig. S8b) as the ending point, where almost all the molecular junctions have broken. Then the individual stretching distance will be used to construct the stretching distance histogram and the peak represents the most probable stretching length of the molecular junctions. Considering the snap-back distance of the gold electrodes determined experimentally to be 0.6–0.8 nm,<sup>9</sup> the corrected elongations of the molecular junction are comparable to the S-S distance in our DFT-optimized molecule structure (Fig. S5).

For molecule **2N-26-2SMe**, the low-G peak cannot be distinguished due to the low junction formation probability. However, a certain number of individual curves exhibit a low conductance plateau around  $10^{-5.5} G_0$ . Thus, we select the ‘signal curve’ based on

the criterion that the stretching distance should be larger than 0.8 nm at  $10^{-5.5} G_0$ . To construct the statistical histogram in Figure 4 in the manuscript. All data without selection is also shown in Figure S12 below.

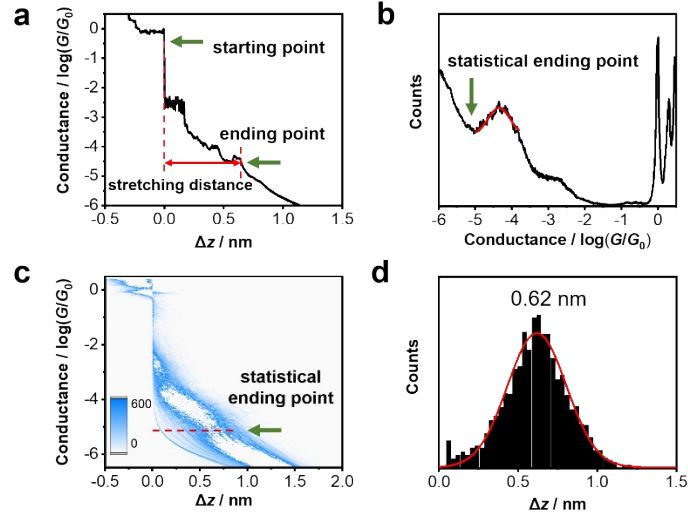


**Figure S8.** Illustration of (a) the stretching distance (b) statistical ending point and the corresponding (c) 2D histogram and (d) plateau length histogram.

### c. Supplemental Single-Molecule Conductance Experiments

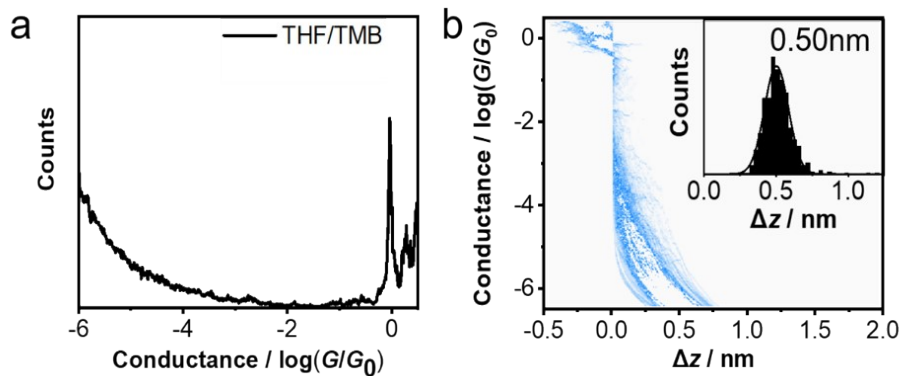


**Figure S9.** (a) 1D and (b) 2D histogram measured in pure solvent and no molecular signal was observed between  $10^{-0.3} G_0$  and  $10^{-6.0} G_0$ .

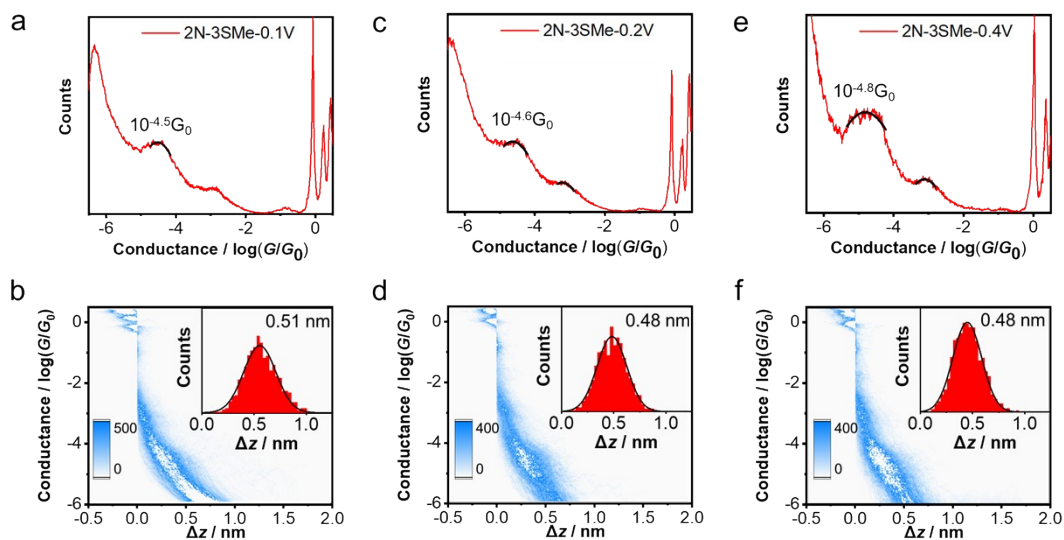


**Figure S10.** Single-molecule conductance results for 2N-3SMe from STM-BJ experiments at three different voltages. (a, c, e) 1D conductance histograms at, respectively. (b, d, f) 2D conductance histograms and the relative-displacement distributions (insets) at 0.1 V, 0.2 V and 0.4 V, respectively.

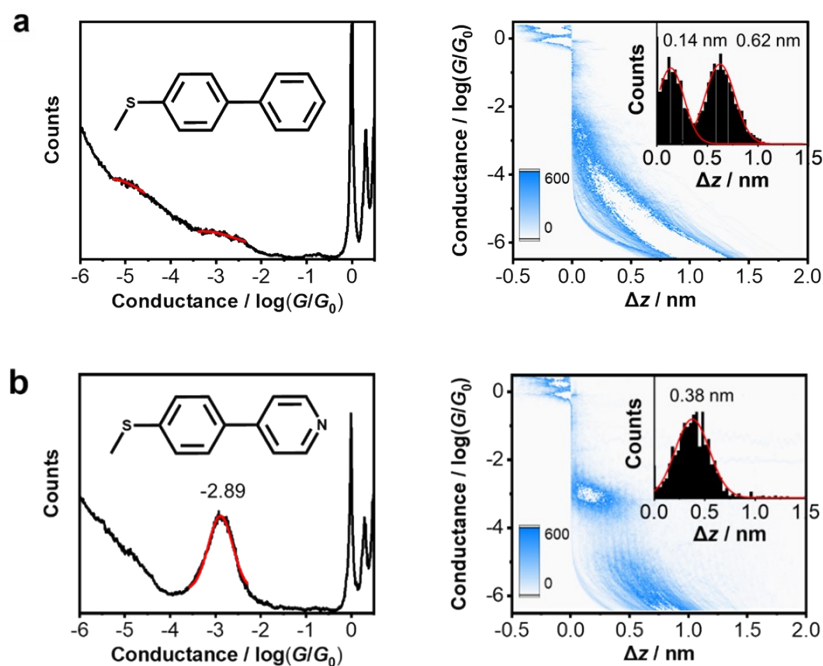


**Figure S11.** Conductance histograms for single-armed molecules (a) **0N-1SMe** (b) **1N-1SMe** for control experiments.

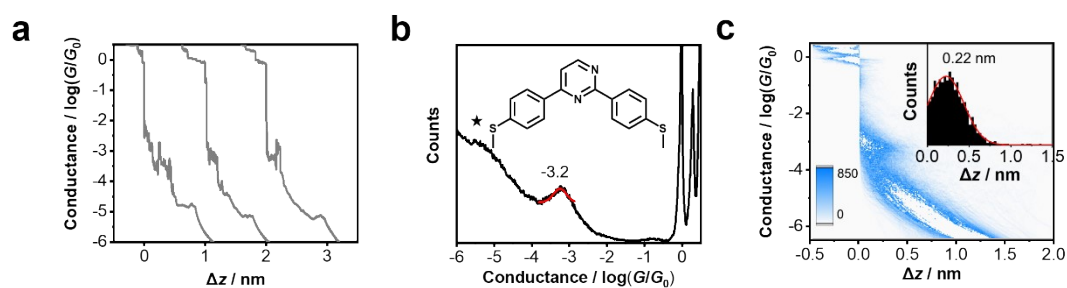


**Figure S12.** STM-BJ results of two-armed molecule **2N-26-2SMe**. (a) Typical individual conductance-displacement traces showing a conductance plateau around  $10^{-5.5} G_0$ . (b) 1D and (c) 2D histograms without data selection. The inset relative stretching displacement histogram is conducted from  $10^{-0.3} G_0$  to  $10^{-3.9} G_0$ .

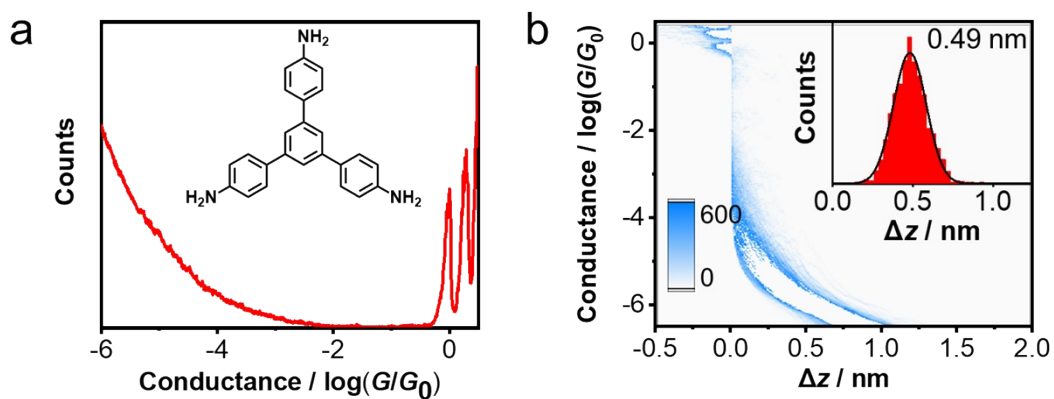


Figure S13. (a) 1D and (b) 2D histogram of molecule 0N-3NH<sub>2</sub>.

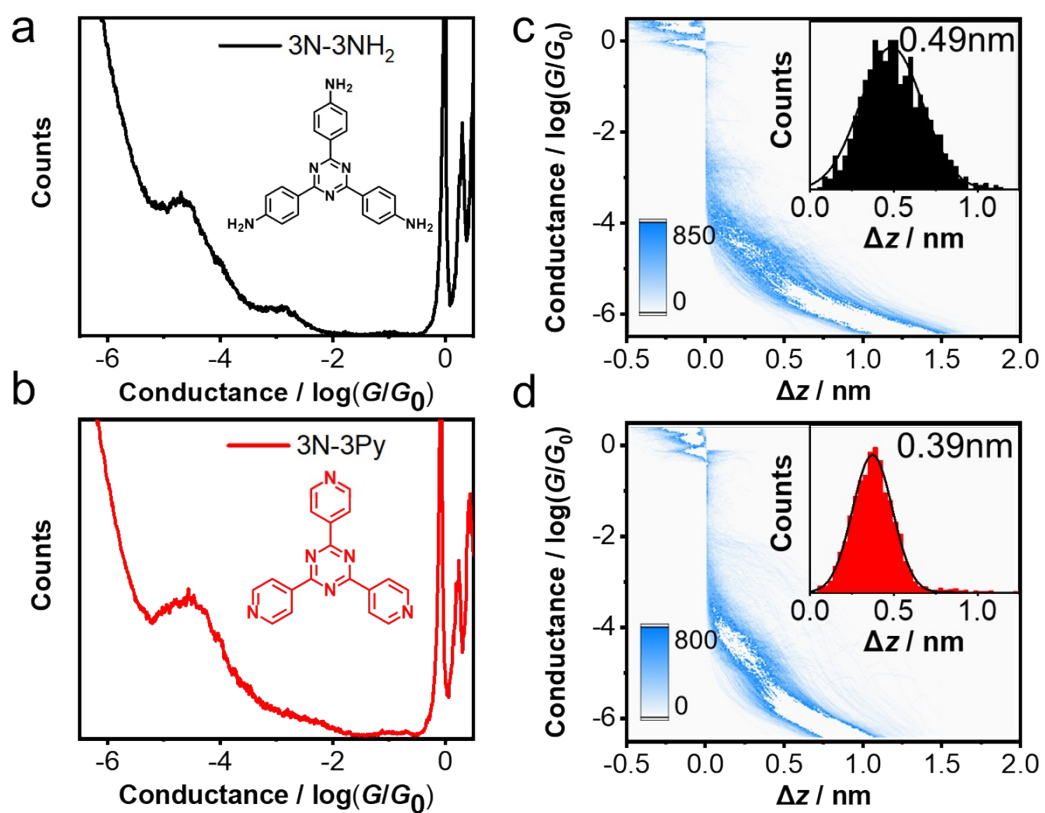


Figure S14. STM-BJ experiment results of 3N substituted molecules the other anchors: (a, c) 3N-3NH<sub>2</sub>. (b, d) 3N-3Py.

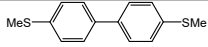
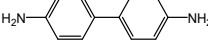
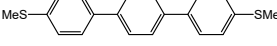
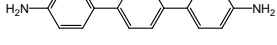
### III. Supplemental Notes

#### a. Discussion about the extremely low conductance of the molecule **0N-NH<sub>2</sub>**

The experimental single-molecule conductance of the **0N-3SMe** molecule is  $10^{5.2\pm 0.3} G_0$ , while the conductance of the molecule **0N-3NH<sub>2</sub>** is below the noise level of our setup ( $<10^{-6.0\pm 0.3} G_0$ ). We consider the extremely low conductance of **0N-3NH<sub>2</sub>** is reasonable and can be interpreted from the following aspects.

On one hand, typically, the anchoring groups can significantly impact the electric coupling between the molecule-electrode interface, thus modulating the electron transport in a single-molecule junction.<sup>10</sup> Taken *para*-linked biphenyl derivatives for example (Table S1), the conductance of the molecules with -SMe anchoring groups are larger than that of the homologous molecules with -NH<sub>2</sub> anchoring groups.

**Table S5.** Experimental single-molecule conductance for *para*-linked biphenyl derivatives

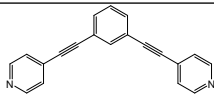
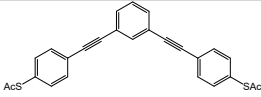
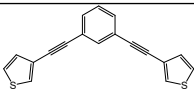
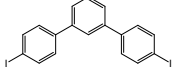
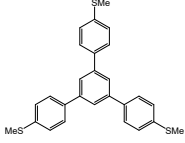
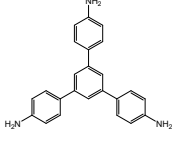
Molecules	Experimental Conductance ( $G_0$ )	Ref.
	around $10^{-2.8}$	2
	around $10^{-3.2}$	2
	$10^{-3.56}$	2
	$10^{-3.97}$	2

On the other hand, previous theoretical work shows that the types of anchoring groups do not fundamentally change the intrinsic DQI which is determined by the core part of the molecule.<sup>11</sup> However, since the DQI anti-resonance feature is so close to the Fermi level that its accurate position plays a decisive role in the low bias conductance of the molecule. This accurate position, certainly, depends on the structure of the molecule (including the core part, the spacer, and the anchoring groups). In MCBJ experiments, for example, single-molecule conductance of *meta*-linked phenyl derivatives with different anchoring groups can span over an order of magnitude,<sup>12-14</sup> which is also summarized in Table S2. In addition, Li *et al*<sup>15</sup> reported that the single-molecule conductance of *m*-terphenyl anchored with iodine atom is  $10^{-4.07} G_0$ , larger by more than one order of magnitude compared with that of **0N-3SMe**. Based on the



reference<sup>16</sup> which shows that the substitution of a benzene ring on 5-position has no significant effect on electronic transport properties, the result by Li *et al* fully indicates that the molecules with DQI structure are very sensitive to the anchoring groups.

**Table S6.** Experimental single-molecule conductance for *meta*-linked phenyl derivatives

Molecules	Experimental Conductance ( $G_0$ )	Ref.
	$10^{-6.0}$	10
	$10^{-5.5}$	11
	$10^{-5.0}$	12
	$10^{-4.1}$	13
	$10^{-5.2}$	this work
	$<10^{-6.0} G_0$	this work

### b. Discussion about the anchor-independent conductance of the 3N series

The counterintuitive phenomenon that the conductance of the 3N molecules with a triazine core is not dependent on the anchoring groups can be understood from two aspects. Firstly, the introduction of three nitrogen atoms significantly alleviated the suppression on electron transport by the DQI effect. The anti-resonance feature has been shifted far away from the Fermi level and even out of the HOMO-LUMO gap. Notably, the transmission function is very smooth, as such the minor structural differences caused by the anchoring groups will not arise dramatic changes in the transmission coefficient at the Fermi level. Secondly, the geometric configurations of 3N series molecules are different from the 0N molecules. In each 0N molecule, the central benzene ring and the adjacent benzene rings have torsional angles (the dihedral angle is about  $38^\circ$  according to our theoretical simulation). The nonplanar configuration

weakens the coupling between the central benzene ring and the surrounding aromatic rings. However, any of the 3N molecules takes a totally planar configuration (the dihedral angle is nearly  $1^\circ\sim 3^\circ$ ), leading to the strong coupling between the central triazine ring and the surrounding aromatic rings. If we regard the central heterocycle as a ‘bridge’ connecting the benzene rings on both sides, the condition is similar to the analysis of the carbazole derivative in the reference by the authors, ‘*the extent to which the orbitals in X interact with the orbitals of the aromatic group determines the strength of the coupling between the sulfur lone pairs in the resulting molecule*’.<sup>17</sup> The strong coupling between the two electrodes and the established conductive pathway endows the 3N molecules with efficient electron transport to the maximum extent.

### c. Comparison with previous work by Solomon et al

Solomon et al investigated theoretically on the novel substitution effect of 1,3-linked benzene by Hückel theory and DFT calculations.<sup>16</sup> They firstly demonstrated that an electron-withdrawing substituent in position 2 can raise the antiresonance energy (the energy where the transmission coefficient is the lowest) while in position 4 (or 6) the antiresonance energy is lowered. The nitrogen atom has greater electronegativity, so its substitution effect is equivalent to an electron-withdrawing group. Our theoretical results for **1N-2** and **1N-4** as well as the trend of experimental conductance are in agreements with the previous work.

For the molecules with two or three substitutional nitrogen atoms, we find that the effect on different positions can be additive, which is also consistent with Solomon’s previous work. The slight difference is the magnitude of the energy shift. Solomon et al found that “*the antiresonance shifts in this unit are close to an integer; for example, the shift for sites 2 and 4 is close to  $-1 \times a$  and  $1 \times a$ , respectively.*” This leads to a complete offset of the substitution effect on 2 and 4 positions and the anti-resonance energy is the same with the meta-linked benzene. However, in our results, the  $G_{rs(HOMO,HOMO-1)}^{(0)}$  and  $G_{rs(LUMO,LUMO+1)}^{(0)}$  are not completely canceled in Table 1. In addition, the contribution of the substitution at site 4 on the energy shift is greater than that at site 2 because the antiresonance energy of **2N-24** molecule is slightly lowered

compared with that of 0N analogue. Nevertheless, our results are consistent with the literature from a qualitative perspective.

#### d. Extended curly arrow rules to rationalize the structural effects on DQI

Curly arrow rules (CARs) can provide chemists with an intuitive method to interpret many observed QI effects. It can be described as follows:<sup>18</sup>

*“Rule 1. Identify the two anchoring units of a molecular wire and replace one with a donor group D and the other with an acceptor group A. If the D lone pair can be delocalized onto A using curly arrows, CQI is expected, if not DQI is expected.”*

In some cases, the CARs may break down when the molecule contains one or more heteroatom(s) such as oxygen and nitrogen. At this time, extended curly arrow rules (ECARs) should be used to repair the breakdown:

*“Rule 2. If DQI is expected, identify any electron-withdrawing groups (EWGs) present in the molecular wire. If EWGs are present, replace each anchor with D. If a lone pair from each D can be independently delocalized to the same EWG, DQI is expected to be shifted away from  $E_F$  (SDQI). Otherwise, DQI is expected around  $E_F$ .”*

Rule 1 (ECAR-1) is a variation of CARs presented previously using D and A groups, and Rule 2 (ECAR-2) is the extension to give ECARs. We apply ECAR-1 and ECAR-2 to understand the substitution effect of the nitrogen atom(s) in our work.

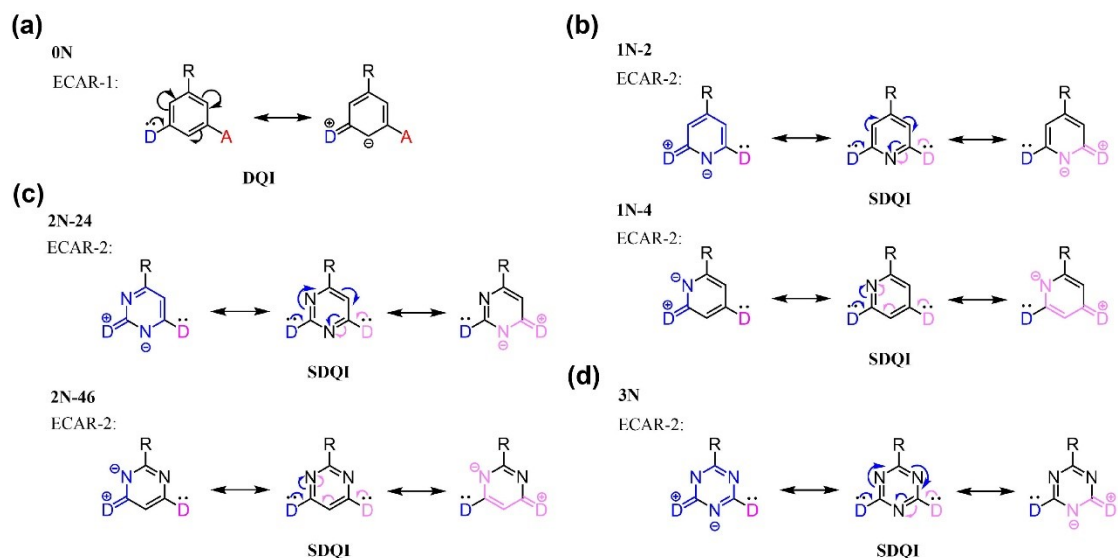


**Figure S15.** Applying ECAR-1 and ECAR-2 to the molecular cores. Here the para-linked 4-(methylthio)phenyl groups are treated as part of the anchoring units.

The ECAR-1 predicts DQI for the molecule **0N-3SMe**. Since the pyridine nitrogen is an electron-withdrawing group, as shown in Figure S15, shifted DQI (SDQI) is predicted for all the other molecules. The limitation of the ECARs is that they cannot quantitatively predict the magnitude of molecular conductance. Nevertheless, the determination of the molecules on DQI or SDQI are qualitatively consistent with our transmission calculation.

#### e. Discussion on the experimental conductance of **3N-3SMe** and **2N-3SMe**

From the single-molecule conductance experiment of two-arm homologous molecules, it can be deduced that the obtained conductance for **2N-3SMe** is originated from **2N-46-3SMe** configuration. This is based on the fact that the junction formation probability of full-stretched **2N-26-2SMe** is very low (25%) and the obtained conductance of **2N-3SMe** is almost exactly the same with that of **2N-46-2SMe**.

The lower conductance of **3N-3SMe** relative to **2N-3SMe** can be understood from the different electronic structures of the central heterocycles, since the DQI feature is their inherent property. The one more nitrogen atom decrease the HOMO and LUMO+1.

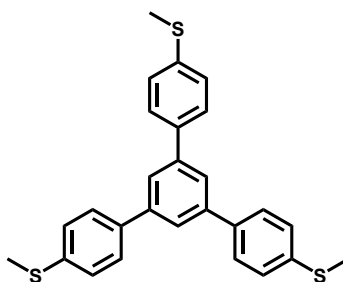
Although the electron density distributions on the anchoring carbon atoms are similar (Fig. S1), the difference in orbital energy (Table S3) enlarges the contribution of HOMOs and shrinks the contribution of LUMOs (Table 1 in main text). It is noted that the sign of  $G_{rs(HOMO, HOMO-1)}^{(0)}$  and  $G_{rs(LUMO, LUMO+1)}^{(0)}$  is opposite, according to orbital symmetry rules,<sup>19, 20</sup> the sum of these two items is smaller for **3N** core. This indicates the destructive interference is more serious in **3N-3SMe** than **2N-3SMe**, consistent with the lower conductance in experiments.

## IV. Synthesis and Characterization of the molecules

### General information

The objective molecules with three anchoring groups (**0N-3SMe**, **1N-3SMe**, **2N-3SMe**, **3N-3SMe**) and their homologous molecules with two anchoring groups (**1N-2-2SMe**, **1N-6-2SMe**, **2N-46-2SMe** and **2N-26-2SMe**) were synthesized by SunaTech Co., Ltd. The molecule **0N-3NH<sub>2</sub>** was synthesized by YanshenTech Co., Ltd. Molecule **3N-3NH<sub>2</sub>** ( $\geq 95\%$ ) is purchased from Aladdin Biochemical Technology Co., Ltd. Molecule **3N-3Py** ( $>97.0\%$ ) is purchased from Tokyo Chemical Industry Co., Ltd. Flash chromatography was performed on silica gel (200-300 mesh). NMR spectra was collected on a Bruker AV III 400 HD (400 MHz). <sup>1</sup>H NMR chemical shifts ( $\delta$ ) are relative to tetramethylsilane. The absolute values of the coupling constants are given in hertz (Hz). Multiplicities are abbreviated as s(singlet), d (doublet), t (triplet), q (quartet), m (multiplet) and br (broad). The high-resolution mass spectra (HRMS) experiments were performed on a Bruker Autoflex III-MALDI-TOF-MS and a Thermo Exactive GC.

## Synthesis and characterization of 0N-3SMe:



The molecule **0N-3SMe** was prepared following the procedure as described for the synthesis of L6.<sup>21</sup> <sup>1</sup>H NMR (400 MHz, Chloroform-*d*)  $\delta$ : 7.70 (s, 3H), 7.63-7.59 (m, 6H), 7.39-7.34 (m, 6H), 2.54 (s, 9H). HRMS(MALDI):  $m/z$  calcd for C<sub>27</sub>H<sub>24</sub>S<sub>3</sub>: 444.1035 [M]<sup>+</sup>; found: 444.1034

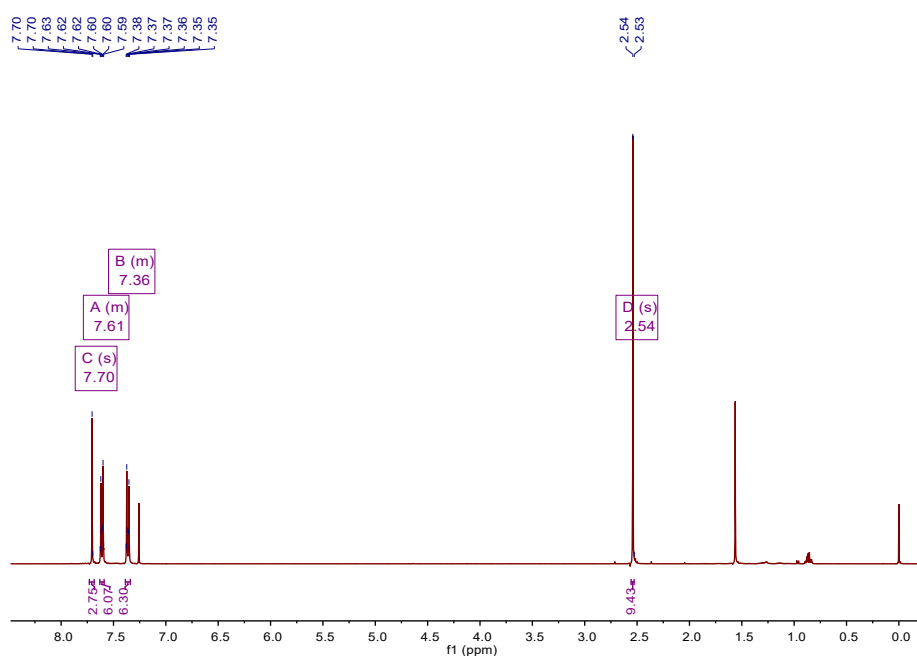


**Fig. S16-1** <sup>1</sup>H NMR spectrum of **0N-3SMe** in chloroform-D

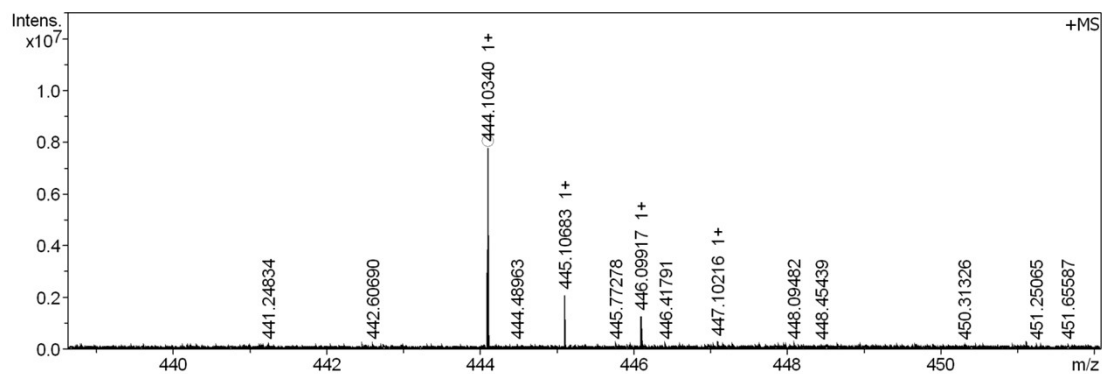
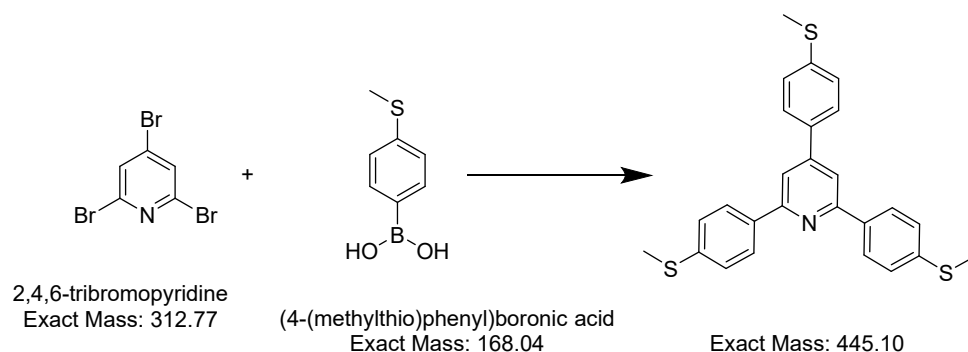


**Fig. S16-2** HRMS(MALDI) spectrum of **0N-3SMe** measured in THF.

### Synthesis and characterization of 1N-3SMe:



A mixture of 2,4,6-tribromopyridine (312 mg, 1.0 mmol), (4-(methylthio)phenyl)boronic acid (756 mg, 4.5 mmol), Pd(dppf)Cl<sub>2</sub> (219 mg, 0.03 mmol), and Na<sub>2</sub>CO<sub>3</sub> (636 mg, 6.0 mmol) in 4 mL of dioxane and 1 mL of water, was stirred at 100°C for 2h, under nitrogen. Then the mixture was diluted with DCM and dried by Na<sub>2</sub>SO<sub>4</sub>. The mixture was concentrated in vacuo. The residue was purified by chromatography (petroleum ether (PE): ethyl acetate (EA)=20:1) to give 286 mg of white solid. The solid was recrystallized from PE and EA to give 106 mg pure product as white solid. The yield was 23.8%. <sup>1</sup>H NMR (400 MHz, Chloroform-*d*) δ: 8.15-8.10 (m, 4H), 7.80 (s, 2H), 7.70-7.64 (m, 2H), 7.38 (dq, J = 8.9, 2.2 Hz, 6H), 2.56 (d, J = 1.9 Hz, 9H). HRMS(MALDI): *m/z* calcd for C<sub>26</sub>H<sub>24</sub>NS<sub>3</sub>: 446.1065 [M+H]; found: 446.1064.

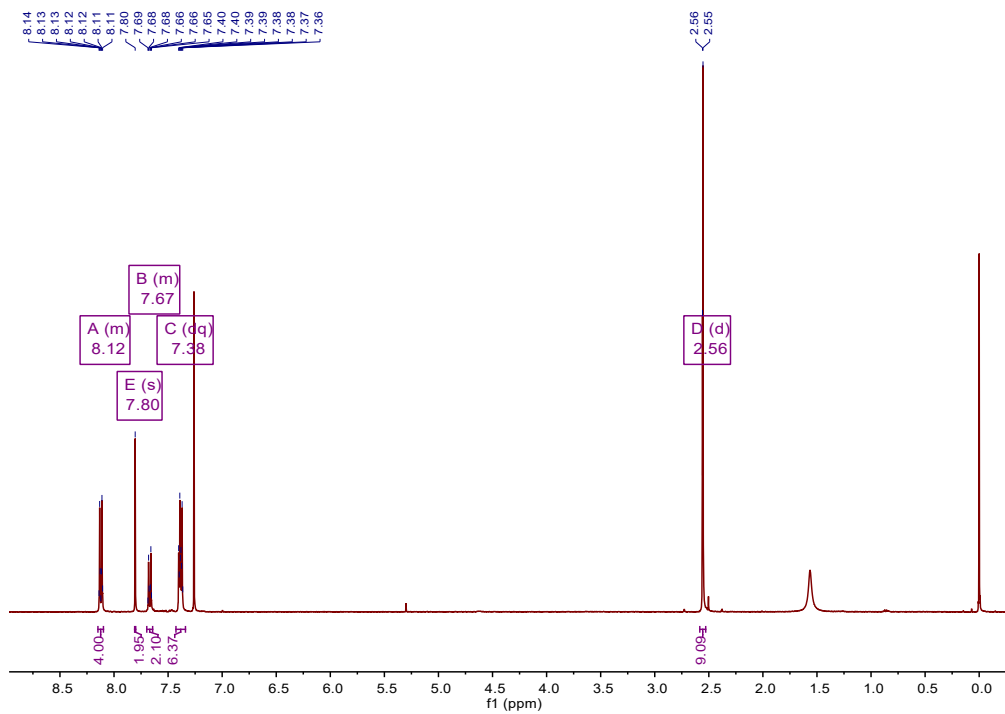


**Fig. S17-1**  $^1\text{H}$  NMR spectrum of **1N-3SMe** in chloroform-D.

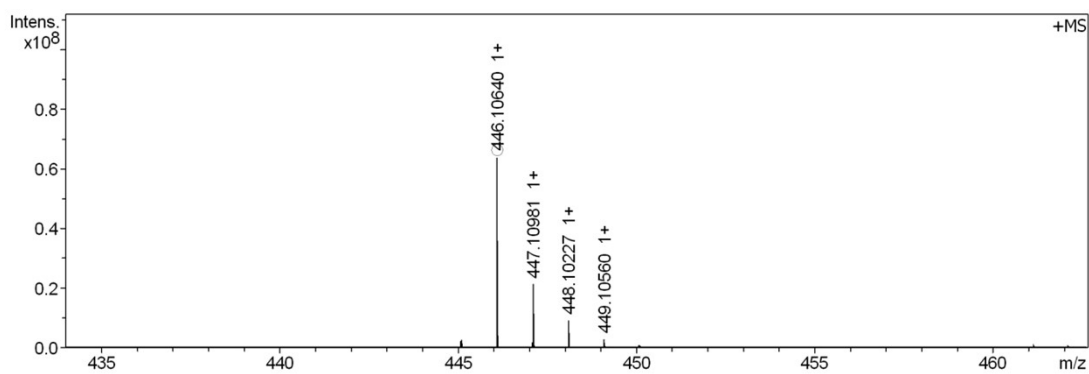
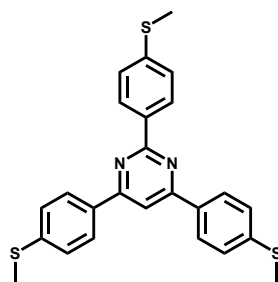


**Fig. S17-2** HRMS(MALDI) spectrum of **1N-3SMe** measured in THF.



## Synthesis and characterization of 2N-3SMe:



The molecule **2N-3SMe** was prepared following the procedure as described for the synthesis of **4**.<sup>22</sup> <sup>1</sup>H NMR (400 MHz, Chloroform-*d*)  $\delta$ : 8.63-8.59 (m, 2H), 8.19 (d, *J* = 8.1 Hz, 4H), 7.89 (s, 1H), 7.38 (dd, *J* = 8.3, 5.3 Hz, 6H), 2.56 (s, 9H). HRMS(MALDI): *m/z* calcd for C<sub>25</sub>H<sub>23</sub>N<sub>2</sub>S<sub>3</sub>: 447.1018 [M+H]<sup>+</sup>; found: 447.1017.

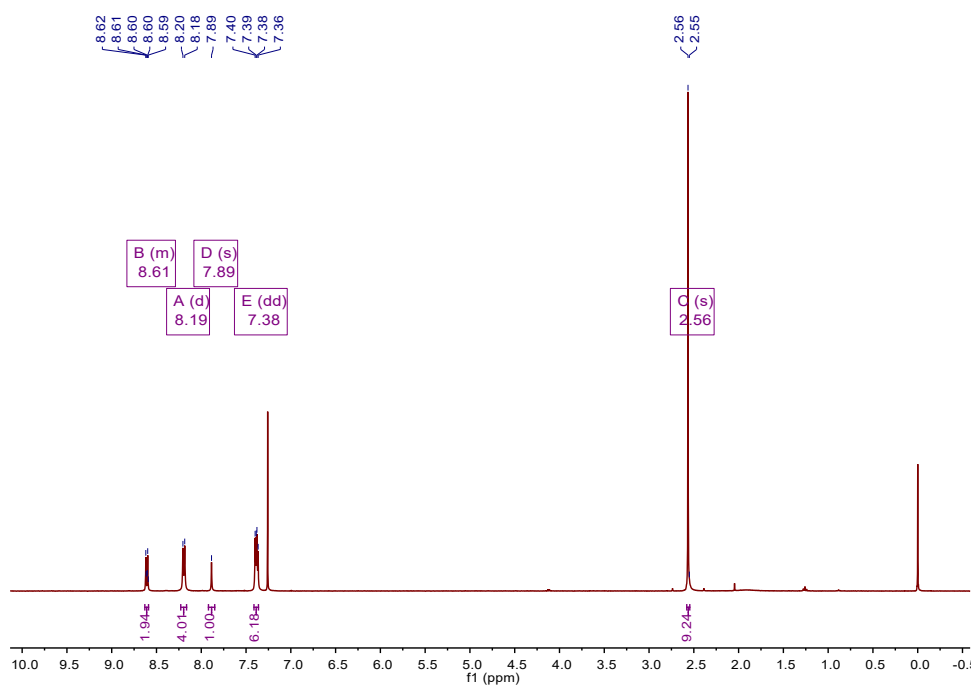


**Fig. S18-1** <sup>1</sup>H NMR spectrum of **2N-3SMe** in chloroform-D.

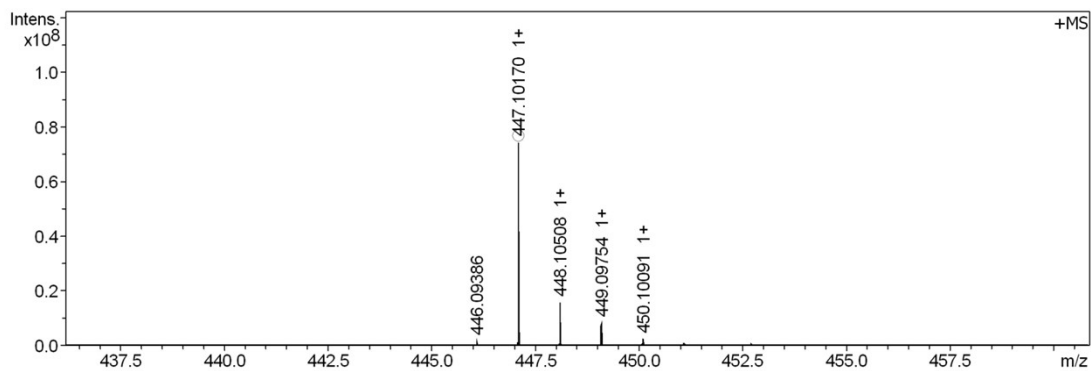
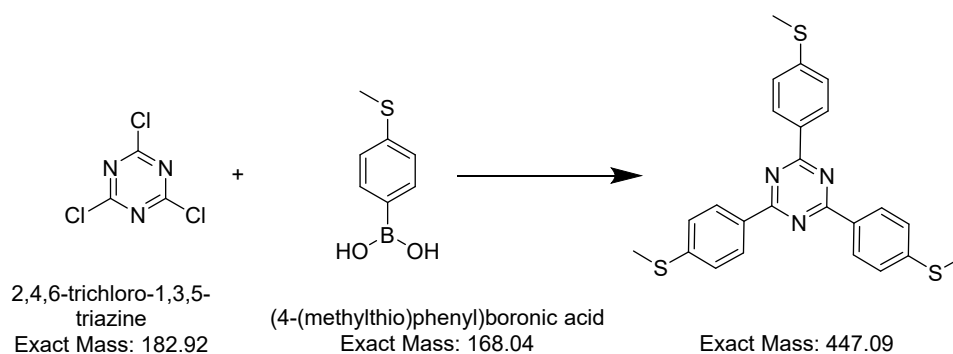


**Fig. S18-2** HRMS(MALDI) spectrum of **2N-3SMe** measured in THF.

### Synthesis and characterization of 3N-3SMe:



A mixture of 2,4,6-trichloro-1,3,5-triazine (183 mg, 1.0 mmol), (4-(methylthio)phenyl)boronic acid (756 mg, 4.5 mmol), Pd(dppf)Cl<sub>2</sub> (219 mg, 0.03 mmol), and Na<sub>2</sub>CO<sub>3</sub> (636 mg, 6.0 mmol) in 4 mL of dioxane and 1 mL of water, was stirred at 100°C for 2h, under nitrogen. Then the mixture was diluted with DCM and dried by Na<sub>2</sub>SO<sub>4</sub>. The mixture was concentrated in vacuo. The residue was purified by chromatography (PE:EA=20:1) to give 260 mg of white solid. The solid was recrystallized from PE and EA to give 110 mg pure product as white solid. The yield was 24.6%. <sup>1</sup>H NMR (400 MHz, Chloroform-*d*) δ: 8.70-8.61 (m, 6H), 7.43-7.35 (m, 6H), 2.58 (s, 9H). HRMS(MALDI): *m/z* calcd for C<sub>24</sub>H<sub>22</sub>N<sub>3</sub>S<sub>3</sub>: 448.0970 [M+H]; found: 448.0970.

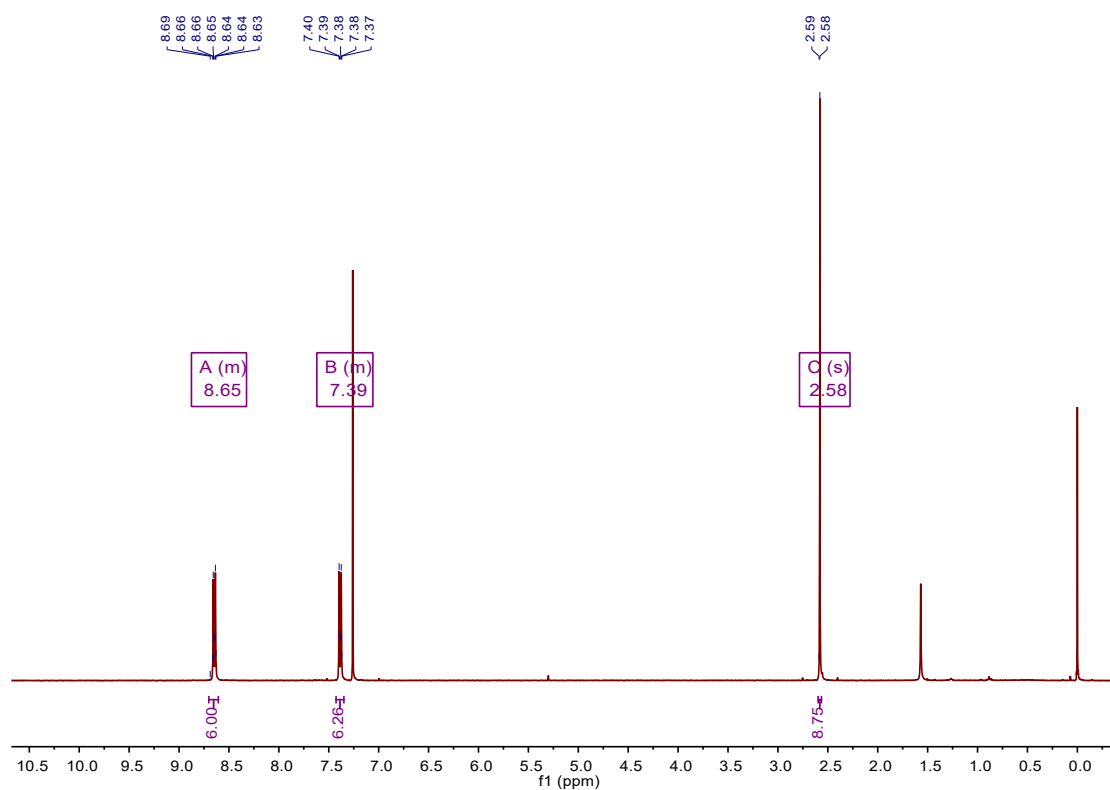


**Fig. S19-1**  $^1\text{H}$  NMR spectrum of **3N-3SMe** in chloroform-D.

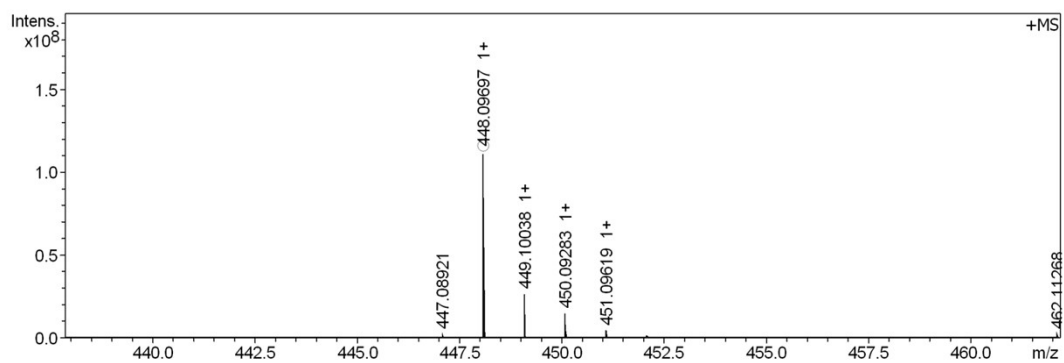
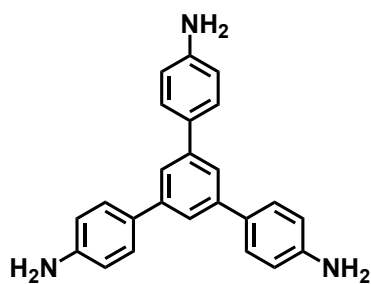


**Fig. S19-2** HRMS(MALDI) spectrum of **3N-3SMe** measured in THF.

**Synthesis and characterization of 0N-3NH<sub>2</sub>:**



The molecule **0N-3NH<sub>2</sub>** was prepared following the procedure as described for the synthesis of Tab.<sup>23</sup> <sup>1</sup>H NMR (400 MHz, DMSO-d<sub>6</sub>) δ 7.48 (s, 6H), 7.46 (d, J = 2.0 Hz, 3H), 6.66 (d, 6H), 5.22 (s, 6H). HRMS(MALDI): *m/z* calcd for C<sub>19</sub>H<sub>21</sub>N<sub>3</sub>: 351.1730 [M]<sup>+</sup>; found: 351.1729.

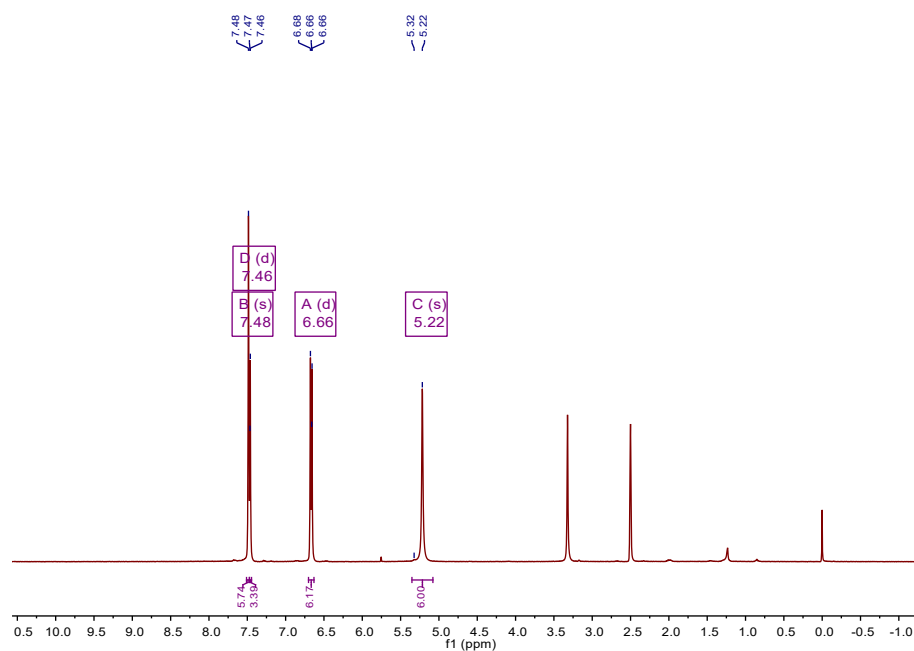


Fig. S20-1  $^1\text{H}$  NMR spectrum of  $0\text{N}-3\text{NH}_2$  in  $\text{DMSO}-\text{D}_6$

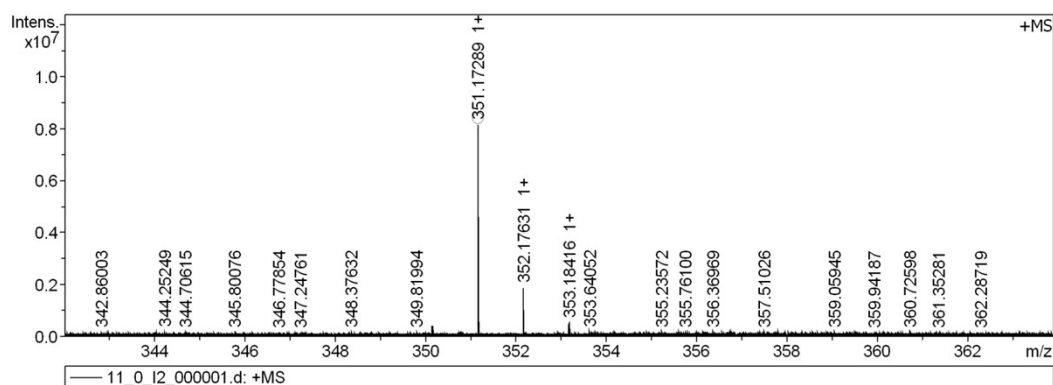


Fig. S20-2 HRMS(MALDI) spectrum of  $0\text{N}-3\text{NH}_2$  measured in THF.

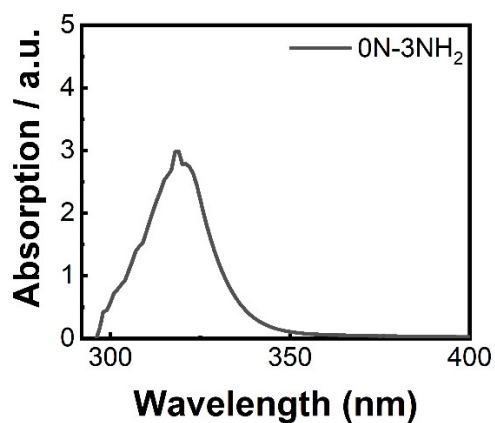
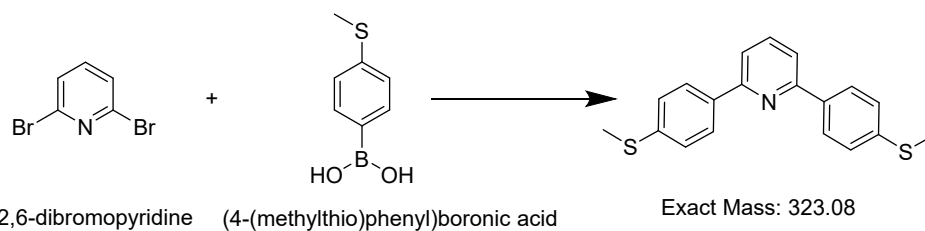
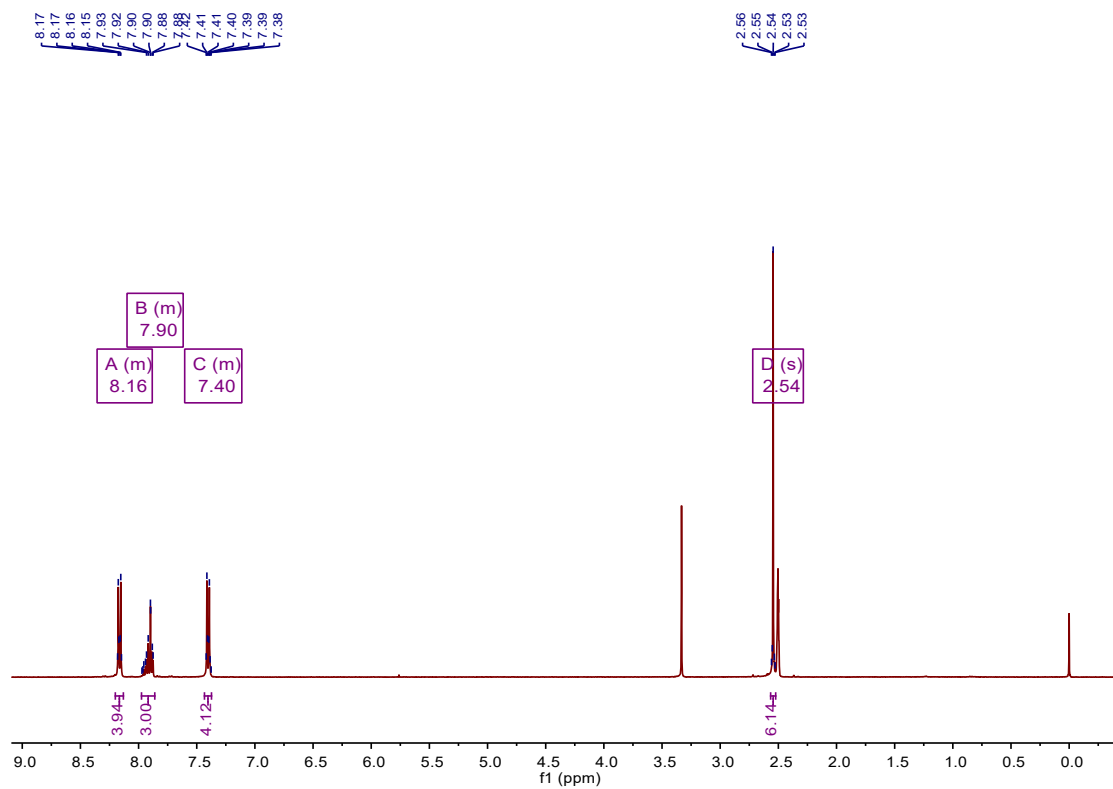


Fig. S20-3. UV-vis spectrum of  $0\text{N}-3\text{NH}_2$  (0.1mM) dissolved in THF: TMB (v: v = 1: 4) solution.

### Synthesis and characterization of 1N-2-2SMe:



A mixture of 2,6-dibromopyridine (234 mg, 1.0 mmol), (4-(methylthio)phenyl)boronic acid (504 mg, 3.0 mmol), Pd(dppf)Cl<sub>2</sub> (73 mg, 0.1 mmol), and Na<sub>2</sub>CO<sub>3</sub> (530 mg, 5.0 mmol) in 4 mL of dioxane and 1 mL of water, was stirred at 100°C for 2h, under nitrogen. Then the mixture was diluted with DCM and dried by Na<sub>2</sub>SO<sub>4</sub>. The mixture was concentrated in vacuo. The residue was purified by chromatography (PE:EA=20:1) to give 245 mg of white solid. The solid was recrystallized from PE and EA to give 95 mg pure product as white solid. The yield was 29.4%. <sup>1</sup>H NMR (400 MHz, DMSO-*d*<sub>6</sub>) δ 8.20-8.13 (m, 4H), 7.97-7.86 (m, 3H), 7.43-7.37 (m, 4H), 2.54 (s, 6H). HRMS(MALDI): *m/z* calcd for C<sub>19</sub>H<sub>18</sub>NS<sub>2</sub>: 324.0875 [M+H]; found: 324.0874.



**Fig. S21-1**  $^1\text{H}$  NMR spectrum of **1N-2-2SMe** in DMSO- $\text{D}_6$ .

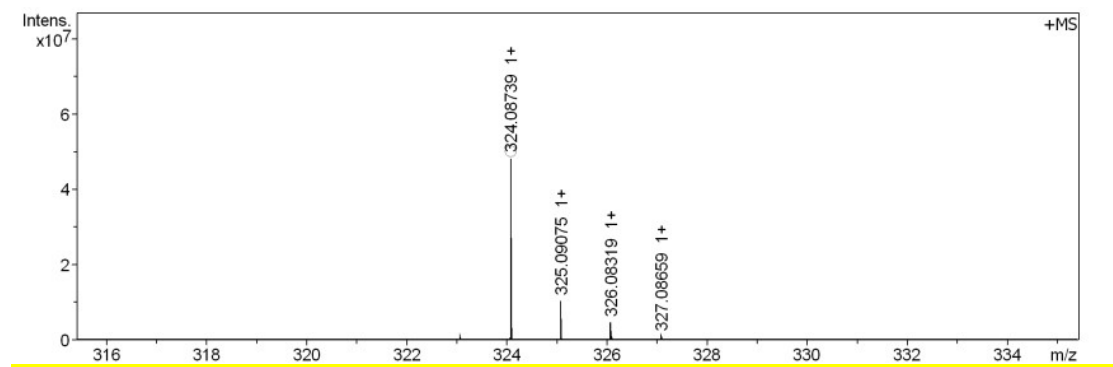
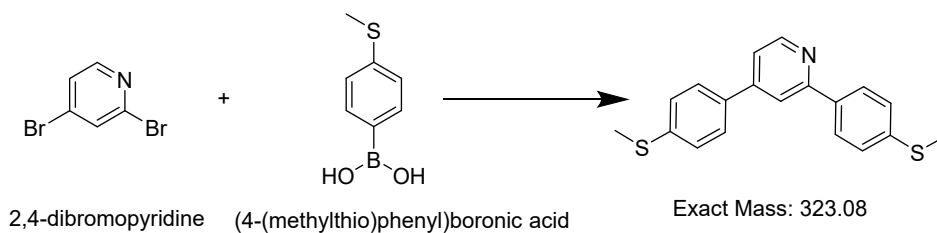


**Fig. S21-2** HRMS(MALDI) spectrum of **2A-1N-2-3SMe** measured in THF.

### Synthesis and characterization of 1N-6-2SMe:



A mixture of 2,4-dibromopyridine (234 mg, 1.0 mmol), (4-(methylthio)phenyl)boronic acid (504 mg, 3.0 mmol), Pd(dppf)Cl<sub>2</sub> (73 mg, 0.1 mmol), and Na<sub>2</sub>CO<sub>3</sub> (530 mg, 5.0 mmol) in 4 mL of dioxane and 1 mL of water, was stirred at 100°C for 2h, under nitrogen. Then the mixture was diluted with DCM and dried by Na<sub>2</sub>SO<sub>4</sub>. The mixture was concentrated in vacuo. The residue was purified by chromatography (PE:EA=20:1) to give 149 mg of white solid. The solid was recrystallized from PE and EA to give 80 mg pure product as white solid. The yield was 24.7%. <sup>1</sup>H NMR (400 MHz, DMSO-*d*<sub>6</sub>) δ 8.67 (d, J = 5.2 Hz, 1H), 8.21 – 8.15 (m, 3H), 7.92 – 7.87 (m, 2H), 7.63 (dd, J = 5.2, 1.7 Hz, 1H), 7.45-7.34 (m, 4H), 2.54 (d, J = 1.8 Hz, 6H). HRMS(MALDI): *m/z* calcd. for C<sub>19</sub>H<sub>18</sub>NS<sub>2</sub>: 324.0785 [M+H]<sup>+</sup>; found: 324.0784.



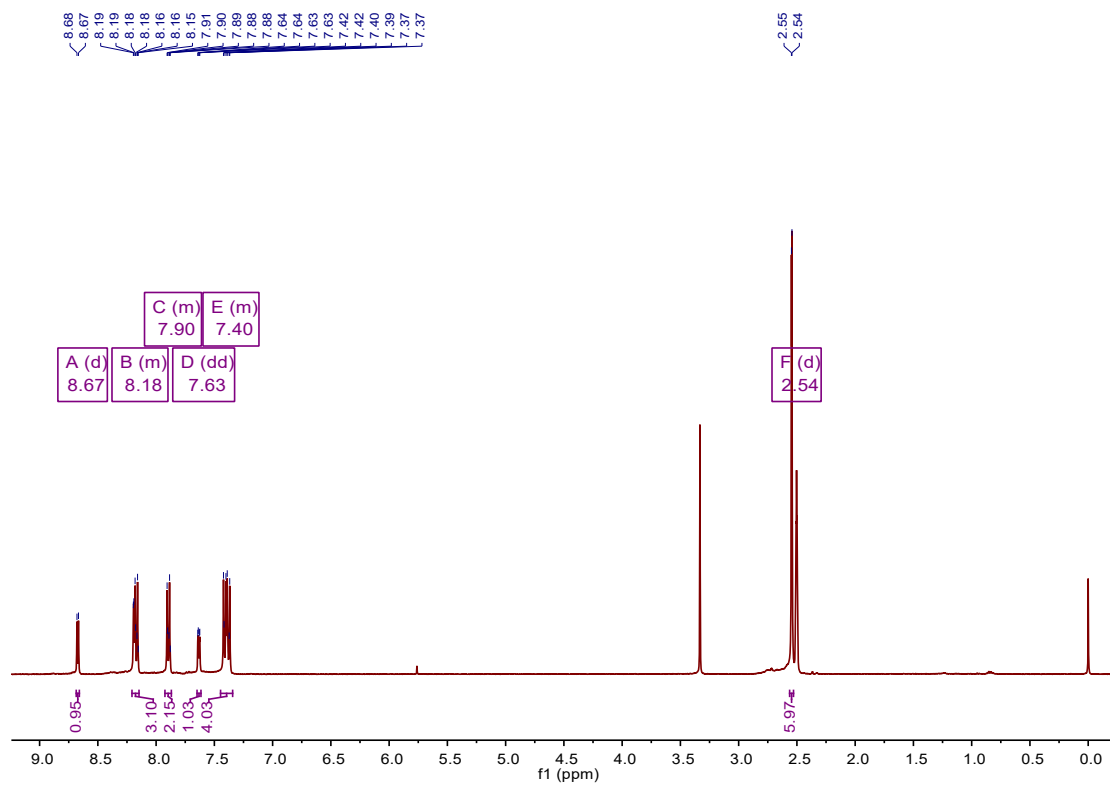


**Fig. S22-1**  $^1\text{H}$  NMR spectrum of **1N-6-2SMe** in DMSO- $\text{D}_6$ .

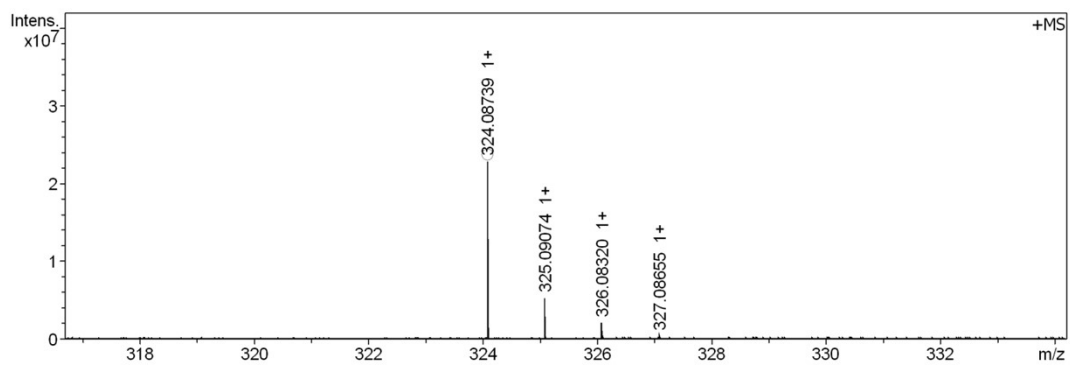
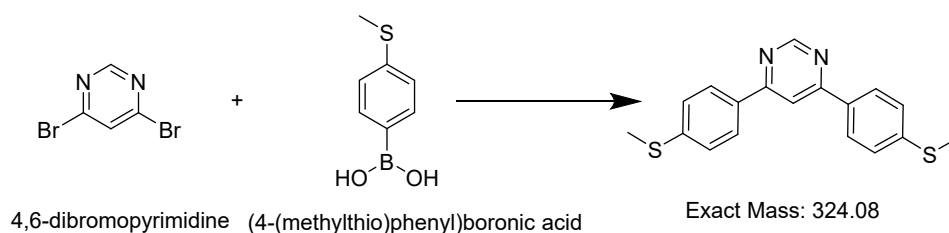


**Fig. S22-2** MS(MALDI) spectrum of **1N-6-2SMe** measured in THF.

### Synthesis and characterization of 2N-46-2SMe:



A mixture of 4,6-dibromopyrimidine (234 mg, 1.0 mmol), (4-(methylthio)phenyl)boronic acid (504 mg, 3.0 mmol), Pd(dppf)Cl<sub>2</sub> (73 mg, 0.1 mmol), and Na<sub>2</sub>CO<sub>3</sub> (530 mg, 5.0 mmol) in 4 mL of dioxane and 1 mL of water, was stirred at 100°C for 2h, under nitrogen. Then the mixture was diluted with DCM and dried by Na<sub>2</sub>SO<sub>4</sub>. The mixture was concentrated in vacuo. The residue was purified by chromatography (PE:EA=20:1) to give 165 mg of white solid. The solid was recrystallized from PE and EA to give 65 mg pure product as white solid. The yield was 20.1%. <sup>1</sup>H NMR (400 MHz, DMSO-*d*<sub>6</sub>) δ: 9.22 (d, J = 1.2 Hz, 1H), 8.56 (d, J = 1.3 Hz, 1H), 8.36-8.28 (m, 4H), 7.47-7.40 (m, 4H), 2.57 (s, 6H). HRMS(MALDI): *m/z* calcd. for C<sub>18</sub>H<sub>17</sub>N<sub>2</sub>S<sub>2</sub>: 325.0828 [M+H]; found: 325.0827.

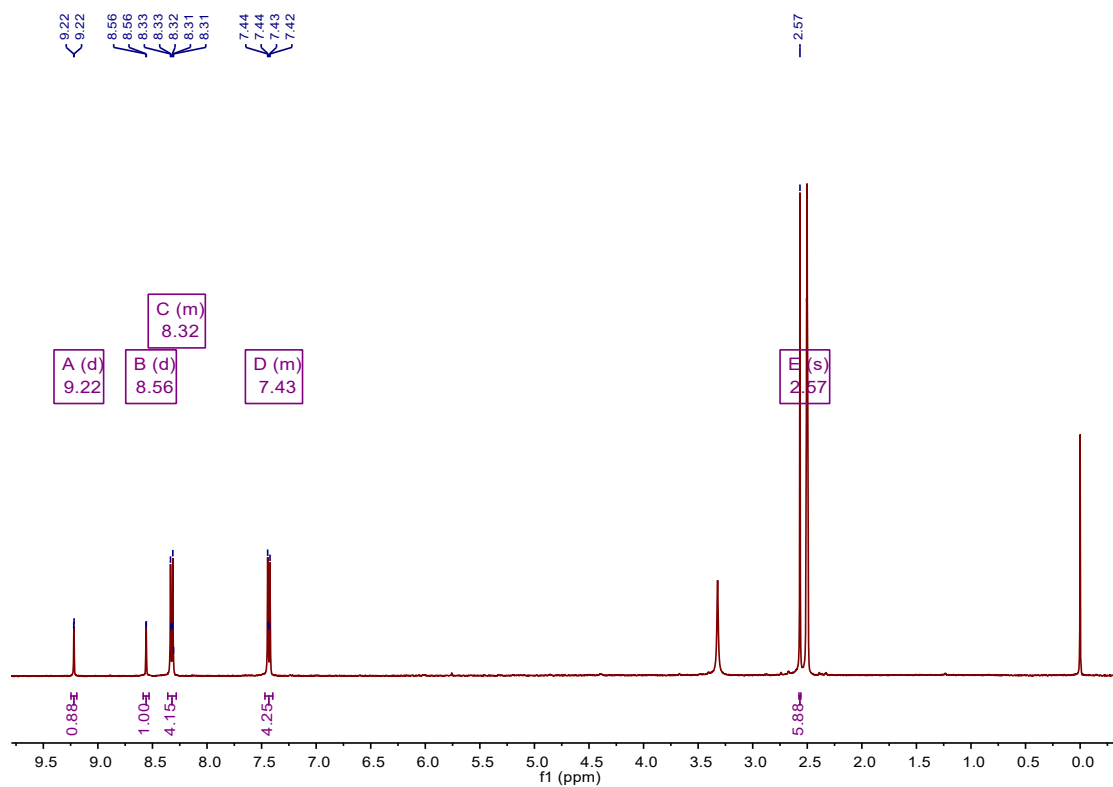


**Fig. S23-1**  $^1\text{H}$  NMR spectrum of 2N-46-2SMe in DMSO-D6.

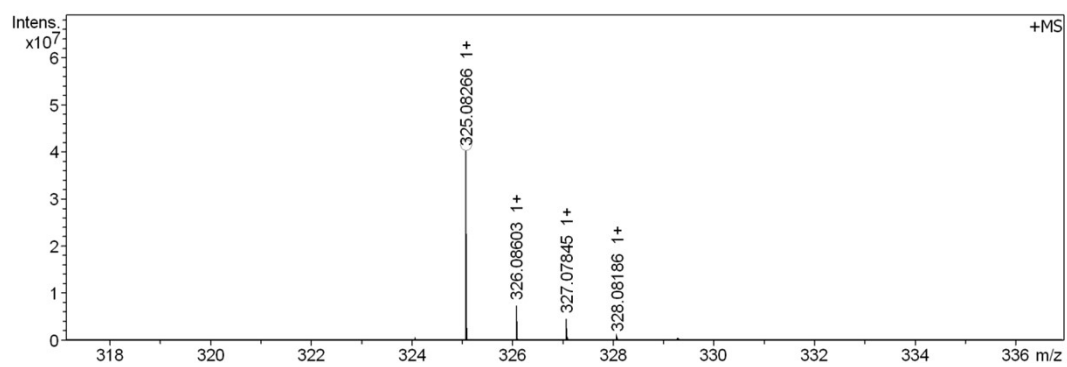
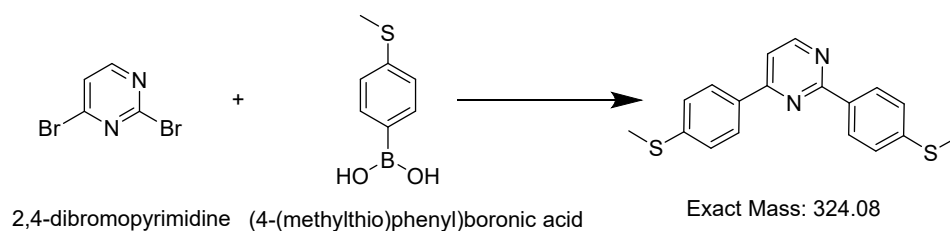


**Fig. S23-2** MS(MALDI) spectrum of 2N-46-2SMe measured in THF.

### Synthesis and characterization of 2N-26-2SMe:



A mixture of 2,4-dibromopyrimidine (234 mg, 1.0 mmol), (4-(methylthio)phenyl)boronic acid (504 mg, 3.0 mmol), Pd(dppf)Cl<sub>2</sub> (73 mg, 0.1 mmol), and Na<sub>2</sub>CO<sub>3</sub> (530 mg, 5.0 mmol) in 4 mL of dioxane and 1 mL of water, was stirred at 100°C for 2h, under nitrogen. Then the mixture was diluted with DCM and dried by Na<sub>2</sub>SO<sub>4</sub>. The mixture was concentrated in vacuo. The residue was purified by chromatography (PE:EA=20:1) to give 205 mg of white solid. The solid was recrystallized from PE and EA to give 102 mg pure product as white solid. The yield was 31.4%. <sup>1</sup>H NMR (400 MHz, DMSO-*d*<sub>6</sub>) δ: 8.89 (d, J = 5.3 Hz, 1H), 8.50-8.41 (m, 2H), 8.32-8.26 (m, 2H), 7.94 (d, J = 5.3 Hz, 1H), 7.47-7.40 (m, 4H), 2.56 (d, J = 2.9 Hz, 6H). HRMS(MALDI): *m/z* calcd. for C<sub>18</sub>H<sub>17</sub>N<sub>2</sub>S<sub>2</sub>: 325.0828 [M+H]; found: 325.0827.

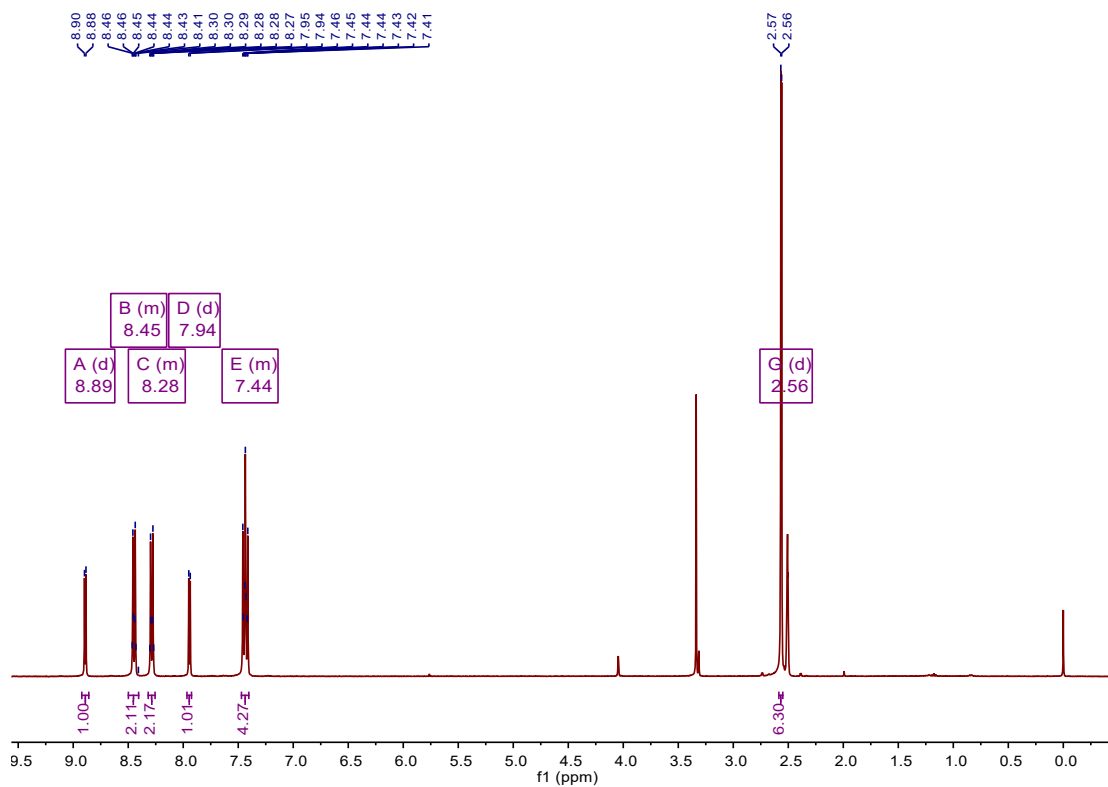


**Fig. S24-1**  $^1\text{H}$  NMR spectrum of **2N-26-2SMe** in DMSO-D<sub>6</sub>.

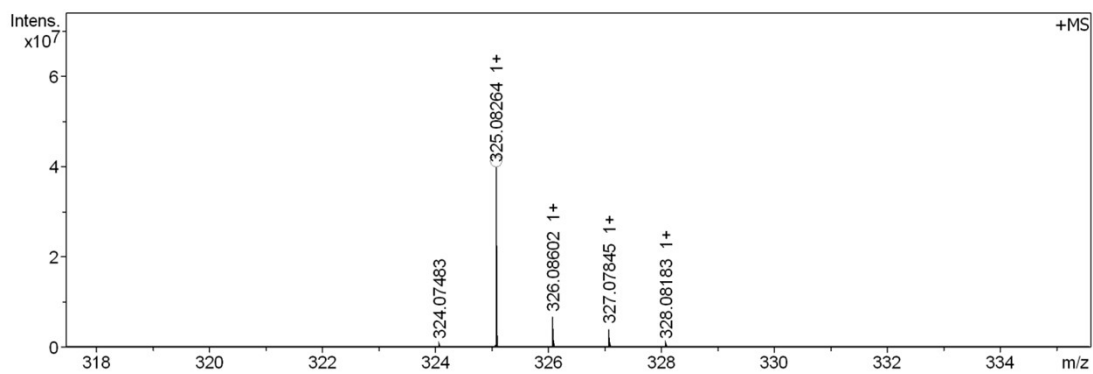
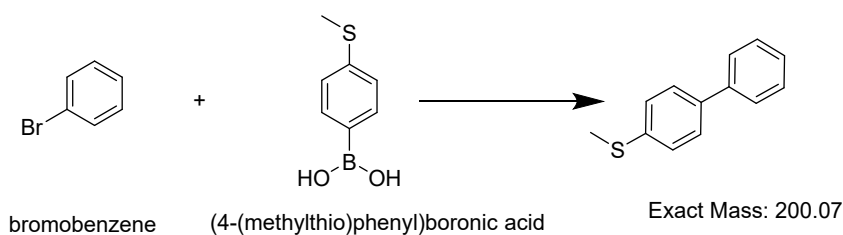


**Fig. S24-2** HRMS(MALDI) spectrum of **2N-26-2SMe** measured in THF.

### Synthesis and characterization of 0N-1SMe:



A mixture of bromobenzene (156 mg, 1.0 mmol), (4-(methylthio)phenyl)boronic acid (253 mg, 1.5 mmol), Pd(dppf)Cl<sub>2</sub> (36 mg, 0.05 mmol), and Na<sub>2</sub>CO<sub>3</sub> (265 mg, 2.5 mmol) in 4 mL of dioxane and 1 mL of water, was stirred at 100°C for 2h, under nitrogen. Then the mixture was diluted with DCM and dried by Na<sub>2</sub>SO<sub>4</sub>. The mixture was concentrated in vacuo. The residue was purified by chromatography (PE:EA=20:1) to give 175 mg of white solid. The solid was recrystallized from PE and EA to give 79 mg pure product as white solid. The yield was 39.5%. <sup>1</sup>H NMR (400 MHz, DMSO-*d*<sub>6</sub>) δ 7.68-7.59 (m, 4H), 7.45 (dd, J = 8.4, 7.0 Hz, 2H), 7.37-7.32 (m, 3H), 2.51 (s, 3H). HRMS(EI): *m/z* calcd C<sub>13</sub>H<sub>12</sub>S: 200.0654 [M]<sup>+</sup>; found: 200.0654.

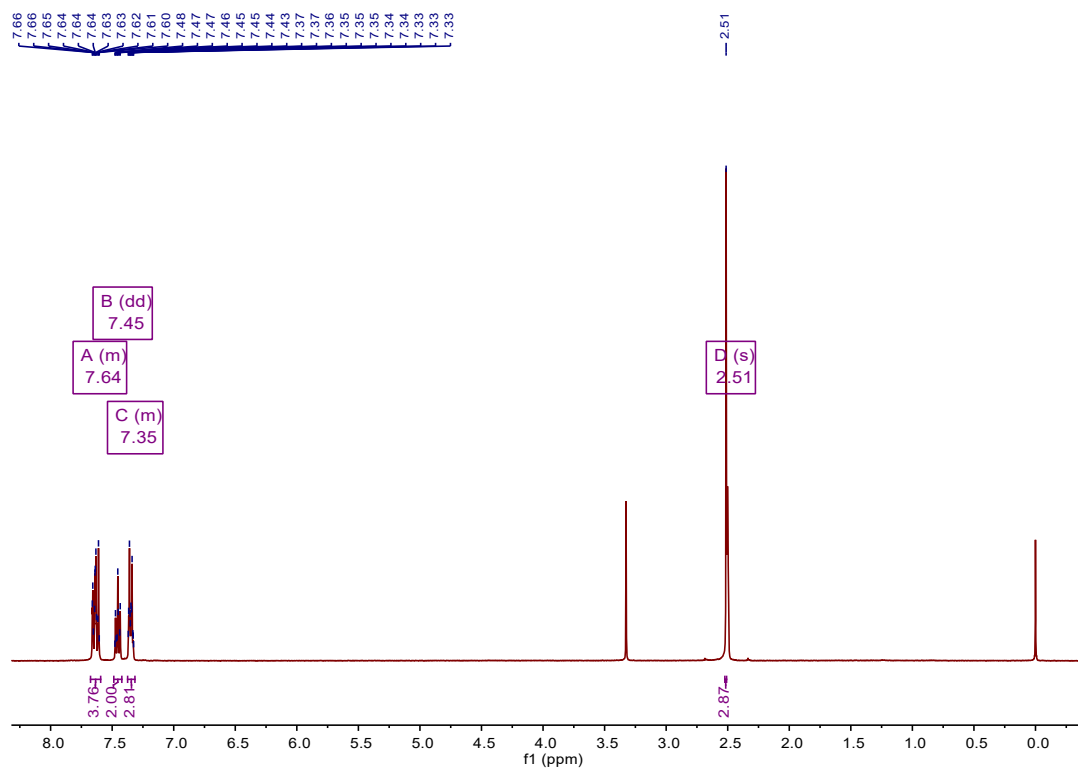


Fig. S25-1  $^1\text{H}$  NMR spectrum of **0N-1SMe** in DMSO- $\text{D}_6$ .

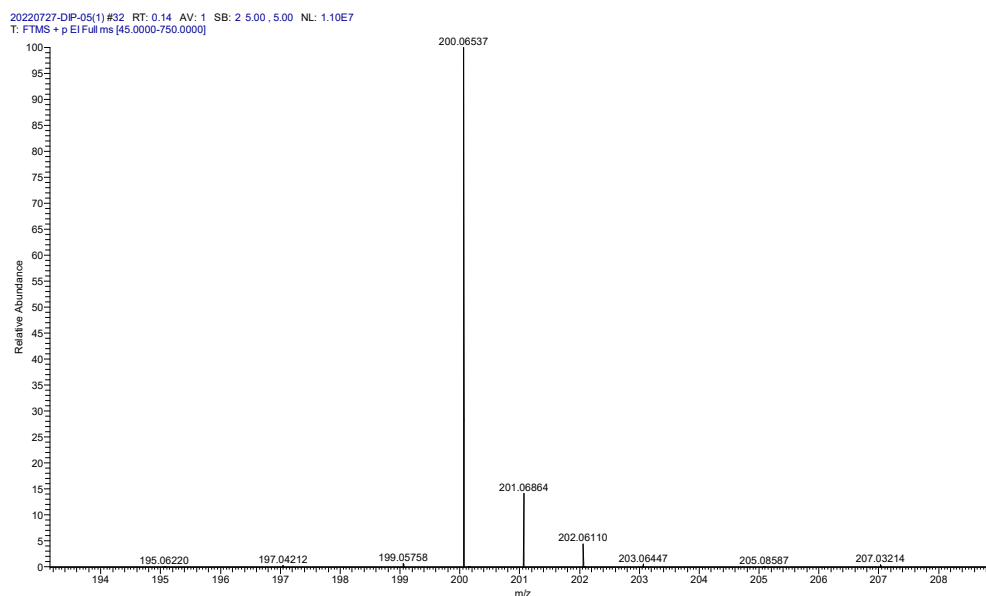
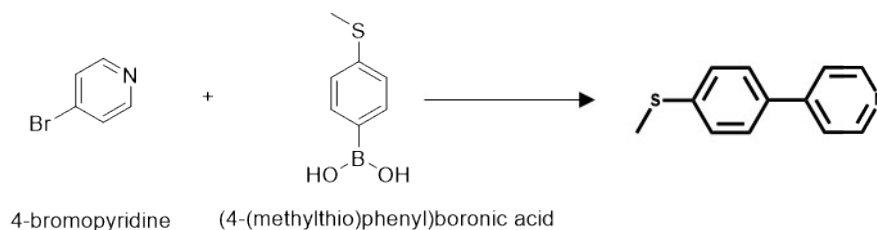


Fig. S25-2 HRMS(EI) spectrum of **0N-1SMe**.

### Synthesis and characterization of 1N-1SMe:



A mixture of 4-bromopyridine (157 mg, 1.0 mmol), (4-(methylthio)phenyl)boronic acid (253 mg, 1.5 mmol), Pd(dppf)Cl<sub>2</sub> (36 mg, 0.05 mmol), and Na<sub>2</sub>CO<sub>3</sub> (265 mg, 2.5 mmol) in 4 mL of dioxane and 1 mL of water, was stirred at 100°C for 2h, under nitrogen. Then the mixture was diluted with DCM and dried by Na<sub>2</sub>SO<sub>4</sub>. The mixture was concentrated in vacuo. The residue was purified by chromatography (PE:EA=20:1) to give 166 mg of white solid. The solid was recrystallized from PE and EA to give 105 mg pure product as white solid. The yield was 52.5%. <sup>1</sup>H NMR (400 MHz, DMSO-*d*<sub>6</sub>) δ 8.65-8.58 (m, 2H), 7.79-7.75 (m, 2H), 7.72-7.68 (m, 2H), 7.43-7.36 (m, 2H), 2.53 (s, 3H). HRMS(MALDI): *m/z* calcd for C<sub>12</sub>H<sub>12</sub>NS: 202.0685 [M+H]; found: 202.0689.



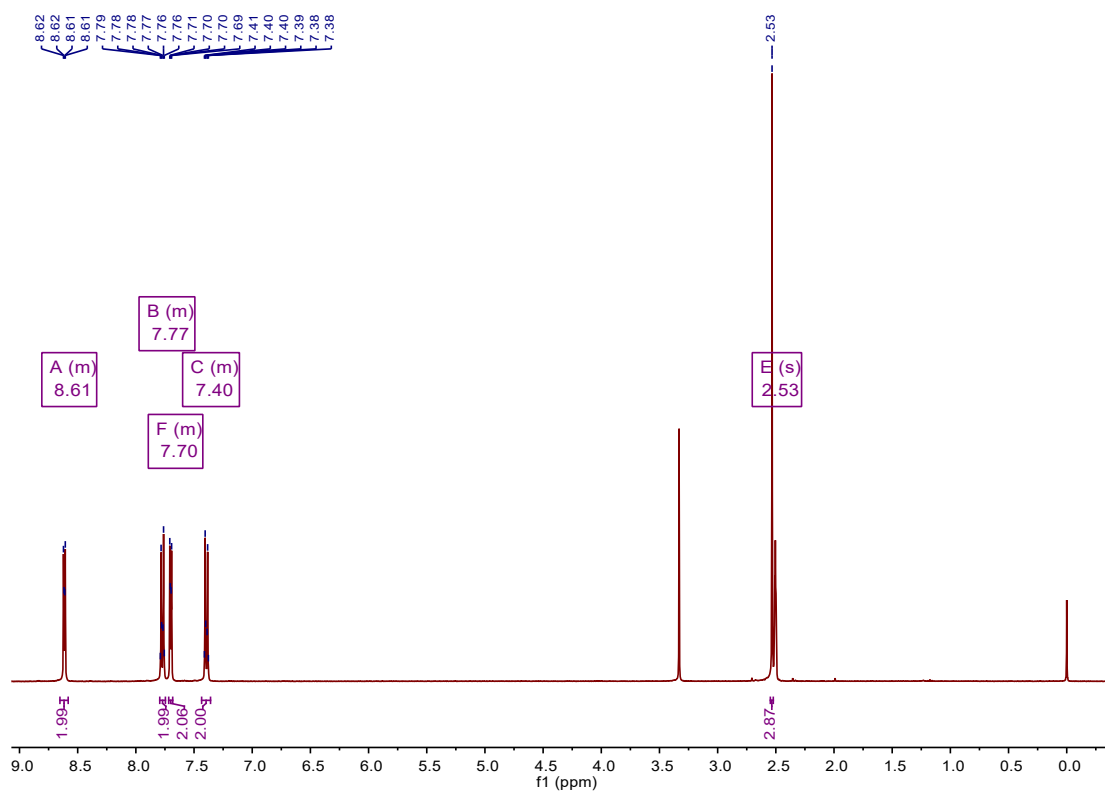


Fig. S26-1  $^1\text{H}$  NMR spectrum of 1N-1SMe in DMSO-D6.

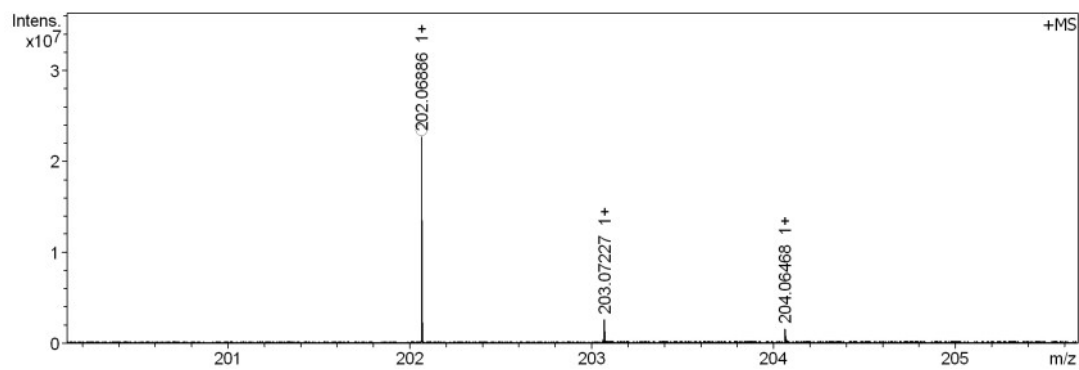


Fig. S26-2 HRMS(MALDI) spectrum of 1N-1SMe measured in THF.

## V. References

1. Carissan, Y.; Hagebaum-Reignier, D.; Goudard, N.; Humbel, S., Hückel-Lewis Projection Method: A “Weights Watcher” for Mesomeric Structures. *The Journal of Physical Chemistry A* **2008**, *112* (50), 13256-13262.
2. Understanding Single-Molecule Parallel Circuits on the Basis of Frontier Orbital Theory. **2020**.
3. Zhang, Y.-P.; Chen, L.-C.; Zhang, Z.-Q.; Cao, J.-J.; Tang, C.; Liu, J.; Duan, L.-L.; Huo, Y.; Shao, X.; Hong, W.; Zhang, H.-L., Distinguishing Diketopyrrolopyrrole Isomers in Single-Molecule Junctions via Reversible Stimuli-Responsive Quantum Interference. *J. Am. Chem. Soc.* **2018**, *140* (21), 6531-6535.
4. Jing, N.; Rui, L.; Xin, S.; Zekan, Q.; Shimin, H.; Rocha, A. R.; Sanvito, S., First-principles calculation on the zero-bias conductance of a gold/1,4-diaminobenzene/gold molecular junction. *Nanotechnology* **2007**, *18* (34), 345203.
5. Li, H.; Garner, M. H.; Shangguan, Z.; Chen, Y.; Zheng, Q.; Su, T.; Neupane, M.; Liu, T.; Steigerwald, M. L.; Ng, F.; Nuckolls, C.; Xiao, S.; Solomon, G. C.; Venkataraman, L., Large Variations in Single Molecule Conductance of Cyclic and Bicyclic Silanes. *J. Am. Chem. Soc.* **2018**, *140* (44), 15080-15088.
6. Hong, W.; Manrique, D. Z.; Moreno-García, P.; Gulcur, M.; Mishchenko, A.; Lambert, C. J.; Bryce, M. R.; Wandlowski, T., Single Molecular Conductance of Tolanes: Experimental and Theoretical Study on the Junction Evolution Dependent on the Anchoring Group. *J. Am. Chem. Soc.* **2011**, *134* (4), 2292-2304.
7. Tang, Y.; Zhou, Y.; Zhou, D.; Chen, Y.; Xiao, Z.; Shi, J.; Liu, J.; Hong, W., Electric Field-Induced Assembly in Single-Stacking Terphenyl Junctions. *J. Am. Chem. Soc.* **2020**, *142* (45), 19101-19109.
8. Kaliginedi, V.; Moreno-García, P.; Valkenier, H.; Hong, W. J.; García-Suárez, V. M.; Buiters, P.; Otten, J. L. H.; Hummelen, J. C.; Lambert, C. J.; Wandlowski, T., Correlations between Molecular Structure and Single-Junction Conductance: A Case Study with Oligo(phenylene-ethynylene)-Type Wires. *J. Am. Chem. Soc.* **2012**, *134* (11), 5262-5275.
9. Kamenetska, M.; Koentopp, M.; Whalley, A. C.; Park, Y. S.; Steigerwald, M. L.; Nuckolls, C.; Hybertsen, M. S.; Venkataraman, L., Formation and Evolution of Single-Molecule Junctions. *Phys. Rev. Lett.* **2009**, *102* (12), 126803.
10. Huang, C.; Rudnev, A. V.; Hong, W.; Wandlowski, T., Break junction under electrochemical gating: testbed for single-molecule electronics. *Chem. Soc. Rev.* **2015**, *44*, 889-901.
11. Tsuji, Y.; Stuyver, T.; Gunasekaran, S.; Venkataraman, L., The Influence of Linkers on Quantum Interference: A Linker Theorem. *J. Phys. Chem. C* **2017**, *121* (27), 14451-14462.
12. Manrique, D. Z.; Huang, C.; Baghernejad, M.; Zhao, X.; Al-Owaedi, O. A.; Sadeghi, H.; Kaliginedi, V.; Hong, W.; Gulcur, M.; Wandlowski, T.; Bryce, M. R.; Lambert, C. J., A quantum circuit rule for interference effects in single-molecule electrical junctions. *Nat. Commun.* **2015**, *6* (1), 6389.
13. Liu, X.; Sangtarash, S.; Reber, D.; Zhang, D.; Sadeghi, H.; Shi, J.; Xiao, Z.-Y.; Hong, W.; Lambert, C. J.; Liu, S.-X., Gating of Quantum Interference in Molecular Junctions by Heteroatom Substitution. *Angew. Chem. Int. Ed.* **2017**, *56* (1), 173-176.
14. Arroyo, C. R.; Tarkuc, S.; Frisenda, R.; Seldenthuis, J. S.; Woerde, C. H. M.; Eelkema, R.; Grozema, F. C.; van der Zant, H. S. J., Signatures of Quantum Interference Effects on Charge Transport

- Through a Single Benzene Ring. *Angew. Chem. Int. Ed.* **2013**, *52* (11), 3152-3155.
15. Li, Y.; Buerkle, M.; Li, G.; Rostamian, A.; Wang, H.; Wang, Z.; Bowler, D. R.; Miyazaki, T.; Xiang, L.; Asai, Y.; Zhou, G.; Tao, N., Gate controlling of quantum interference and direct observation of anti-resonances in single molecule charge transport. *Nat. Mater.* **2019**, *18* (4), 357-363.
  16. Garner, M. H.; Solomon, G. C.; Strange, M., Tuning Conductance in Aromatic Molecules: Constructive and Counteractive Substituent Effects. *J. Phys. Chem. C* **2016**, *120* (17), 9097-9103.
  17. Klausen, R. S.; Widawsky, J. R.; Su, T. A.; Li, H.; Chen, Q.; Steigerwald, M. L.; Venkataraman, L.; Nuckolls, C., Evaluating atomic components in fluorene wires. *Chem. Sci.* **2014**, *5* (4), 1561-1564.
  18. O'Driscoll, L. J.; Bryce, M. R., Extended curly arrow rules to rationalise and predict structural effects on quantum interference in molecular junctions. *Nanoscale* **2021**, *13* (2), 1103-1123.
  19. Yoshizawa, K., An Orbital Rule for Electron Transport in Molecules. *Acc. Chem. Res.* **2012**, *45* (9), 1612-1621.
  20. Yoshizawa, K.; Tada, T.; Staykov, A., Orbital Views of the Electron Transport in Molecular Devices. *J. Am. Chem. Soc.* **2008**, *130* (29), 9406-9413.
  21. Huang, G.; Sun, Y. Q.; Xu, Z.; Zeller, M.; Hunter, A. D., Structural regularity and diversity in hybrids of aromatic thioethers and BiBr<sub>3</sub>: from discrete complexes to layers and 3D nets. *Dalton Trans* **2009**, (26), 5083-93.
  22. Achelle, S.; Ramondenc, Y.; Marsais, F.; Plé, N., Star- and Banana-Shaped Oligomers with a Pyrimidine Core: Synthesis and Light-Emitting Properties. *Eur. J. Org. Chem.* **2008**, (18), 3129-3140.
  23. Sun, Q.; Aguila, B.; Perman, J.; Earl, L. D.; Abney, C. W.; Cheng, Y.; Wei, H.; Nguyen, N.; Wojtas, L.; Ma, S., Postsynthetically Modified Covalent Organic Frameworks for Efficient and Effective Mercury Removal. *J Am Chem Soc* **2017**, *139* (7), 2786-2793.